



Suspended sediment transport under seiches in circular and elliptical basins

David Pritchard^a, Andrew J. Hogg^{b,*}

^a*B.P. Institute for Multiphase Flow, University of Cambridge, Madingley Rise, Madingley Road, Cambridge CB3 0EZ, England, UK*

^b*Centre for Environmental and Geophysical Flows, Department of Mathematics, University of Bristol, Bristol BS8 1TW, England, UK*

Received 22 August 2002; received in revised form 22 April 2003; accepted 28 May 2003

Abstract

Enclosed bodies of water such as lakes or harbours often experience large-scale oscillatory motions (seiching). As a simple model of such flow, we investigate exact solutions to the shallow-water equations which represent oscillatory flow in an elliptical basin with parabolic cross section. Specifically, we consider two fundamental modes of oscillation, in one of which the flow is parallel to the axis of the ellipse, while in the other it is radial. We obtain periodic analytical solutions for sediment transport, including erosion, deposition and advection, under either mode of oscillation, and present a method for obtaining such solutions for a more general class of flow fields and sediment transport models.

Our solutions provide estimates of the morphodynamical importance of seiching motions and also reveal a characteristic pattern of net erosion and deposition associated with each mode. In particular, we find that a net flux of suspended sediment can be transported from the deeper to the shallower regions of the basin. These transport patterns, which are driven essentially by settling lag, are highly robust to the formulation of the sediment transport relation and appear not to be substantially affected by the omission of frictional terms in the hydrodynamics: they should thus provide considerable insight into sediment transport in less-idealised systems.

© 2003 Elsevier B.V. All rights reserved.

Keywords: Shallow-water environment; Nearshore sedimentation; Sand; Silt; Cyclic processes

1. Introduction

The processes by which sediment is mobilised and redistributed in confined bodies of water such as harbours, lagoons and lakes are naturally of considerable interest to the coastal and civil engineer, as well as to the sedimentologist or limnologist. In

particular, an understanding of these processes is necessary in order to predict and control the morphological evolution of such systems, with potentially important ecological and navigational consequences. To date, these topics have been addressed almost exclusively through empirical and numerical studies, and the object of this paper is to complement such studies with a theoretical investigation of some of the mechanisms involved.

We approach the problem by developing exact solutions for the suspended sediment field in the water body under specific types of hydrodynamic forcing.

* Corresponding author.

E-mail addresses: david@bpi.cam.ac.uk (D. Pritchard), a.j.hogg@bristol.ac.uk (A.J. Hogg).

These solutions are useful in two respects. Firstly, they offer insight into the physical processes which control sediment redistribution, in a clearer form than may readily be obtained from field data or from extensive numerical simulations. Secondly, they provide easily reproduced test cases which may be used to validate numerical models for the prediction of sediment transport. We now discuss each of these points in turn.

In a confined body of water, bedload transport, in the form of either granular flows of noncohesive material (see, e.g. [Seminara, 2001](#)) or fluid mud layers (e.g. [Roberts, 1993](#); [Ali et al., 1997](#)), is directed preferentially downslope into the deeper regions in the middle of the basin. Other mechanisms such as sediment focussing by secondary circulation are also known to contribute to this net inward movement of sediment ([Bloesch, 1995](#)). However, it is less obvious how or whether there is some return flux of suspended sediment into the shallower regions of the basin—a question which is clearly of considerable importance for the morphodynamics of the system.

One obvious candidate mechanism for such transport is wind-generated waves and the associated currents, which may be expected to be particularly important where the water is relatively shallow. However, when considering transport in deeper regions, it is necessary to examine the possible effects of other hydrodynamic processes. In particular, both internal and surface seiche motions have been proposed as possible mechanisms for sediment reworking and transport in studies of contemporary and historical sedimentation (see, for example, [Bloesch, 1995](#); [Shteynman et al., 1997](#); [Chapon et al., 1999](#)), and there is therefore a useful role to be played by a theoretical investigation of such transport. The current study is complementary to recent investigations of the role of suspended sediment transport on tidal flats ([Pritchard et al., 2002](#); [Pritchard and Hogg, submitted for publication \(a\)](#)) and in tidal inlets ([Schuttelaars and de Swart, 1996, 1999](#); [Schuttelaars, 1998](#)).

In the current study, we confine ourselves to considering surface seiches in a somewhat idealised geometry. The advantage of this approach is that we are able to employ the exact solutions for the nonlinear normal modes of oscillation of fluid in a basin of parabolic cross section which were derived by [Thacker \(1981\)](#) and thus to obtain exact analytical

solutions for suspended sediment transport. This allows a clearer and somewhat more thorough investigation of the transport mechanisms than a purely numerical study.

A particular difficulty encountered in numerical models of nearshore hydrodynamics and sediment transport is the representation of the variables in shallow water close to the moving shoreline. In order to obtain reliable results in this region, it is essential that numerical methods be validated both against field data and against exact solutions where these are available. There is, however, a scarcity of available solutions for such validation even for the hydrodynamic fields and even fewer for the suspended sediment field: this therefore represents an important secondary motivation for the work described here. A particular feature of the Lagrangian approach, which we employ to develop our solutions, is that the moving shoreline boundary may be handled without the need to impose extra physical or numerical conditions on the suspended sediment concentration here.

In this paper, we compare the sediment transport under two basic modes of oscillation of the fluid body. In one, the basin is elliptical in plan view, and the fluid motion is parallel to one axis of the ellipse; in the other, the basin is circular in plan view, and the fluid motion is radial. A distinct pattern of net sediment transport is associated with each mode: axial flow transports material outwards from the centre and deposits it in the shallower parts of the basin, while radial flow erodes material from an annular region and deposits it principally landwards of this region. The robustness of these results suggests that they offer genuine insight into how such oscillations may contribute to long-term patterns of sediment movement and thus to morphological change.

In Section 2, we introduce the shallow-water equations which describe the fluid motion and sediment transport. In particular, we describe a model for the erosion and deposition of sediment which is principally intended to represent coarse sand, but which may easily be adapted to finer and even to cohesive sediment. In Section 3, we consider axial oscillations in an elliptical basin, and in Section 4, we consider radial oscillations in a circular basin. In both sections, exact periodic solutions to the sediment transport equation are constructed using the general method described in Appendix A. Finally, in Section

5, we summarise our results and discuss their implications for more general bathymetries. Appendix B deals briefly with the extent to which the neglect of friction in obtaining these results may be justified.

2. Description of the model

Throughout this study, we are concerned with basins which have the form

$$\hat{d}(\hat{x}, \hat{y}) = \hat{D}_0 \left(1 - \frac{\hat{x}^2}{\hat{D}_x^2} - \frac{\hat{y}^2}{\hat{D}_y^2} \right), \quad (1)$$

where \hat{x} and \hat{y} are orthogonal horizontal coordinates and where \hat{d} represents the vertical depth of the bed below an arbitrary datum. We assume that the horizontal extent of the basin in the \hat{x} - and \hat{y} -directions is similar, $\hat{D}_x/\hat{D}_y = \mathcal{O}(1)$. (Here and throughout, carets $\hat{\cdot}$ and bars $\bar{\cdot}$ denote dimensional quantities, and the nondimensional variables which are introduced below are unadorned.)

Fig. 1 illustrates the flows which we will consider.

The region occupied by fluid is bounded by the instantaneous shoreline, which consists of a set of points $\hat{\mathbf{x}}_{sh}(t)$: in subsequent sections, it will be possible either to express the shoreline in terms of a single radial coordinate, $\hat{r} = \hat{r}_{sh}(\hat{t})$, or in terms of a simple relationship between the Cartesian coordinates $\hat{x}_{sh}(\hat{t})$ and $\hat{y}_{sh}(\hat{t})$.

2.1. Hydrodynamics

We employ the shallow-water formulation for the hydrodynamics which has been employed in many other recent studies of coastal and estuarine sediment

transport. This formulation is based on the assumption that the horizontal extent of the flow is large compared to its depth (Peregrine, 1972), which for the flows we consider here is generally satisfied.

The hydrodynamics are then described in terms of the vertically averaged velocities in the \hat{x} - and \hat{y} -directions,

$$\bar{\mathbf{u}}(\hat{x}, \hat{y}, \hat{t}) = \frac{1}{\hat{h}} \int_{-\hat{d}}^{\hat{h}-\hat{d}} \hat{\mathbf{u}}(\hat{x}, \hat{y}, \hat{z}, \hat{t}) d\hat{z}, \quad (2)$$

where $\hat{\mathbf{u}} = (\hat{u}, \hat{v})$ and where $\hat{h}(\hat{x}, \hat{y}, \hat{t})$ is the total depth of fluid at a point. We nondimensionalise these quantities with respect to a horizontal length scale \hat{L}_h which we identify with \hat{D}_x , a vertical length scale $\hat{L}_z \ll \hat{L}_x$ which we identify with \hat{D}_0 , and a time scale $\hat{T}_0 = \hat{D}_x/(\hat{g}\hat{D}_0)^{1/2}$. In nondimensional form, then, the shallow-water equations in two dimensions are

$$\frac{\partial h}{\partial t} + \frac{\partial}{\partial x}(uh) + \frac{\partial}{\partial y}(vh) = 0, \quad (3)$$

$$\frac{\partial u}{\partial t} + u \frac{\partial u}{\partial x} + v \frac{\partial u}{\partial y} + \frac{\partial}{\partial x}(h-d) = 0, \quad (4)$$

$$\frac{\partial v}{\partial t} + u \frac{\partial v}{\partial x} + v \frac{\partial v}{\partial y} + \frac{\partial}{\partial y}(h-d) = 0. \quad (5)$$

In this formulation of the shallow-water equations, we have assumed that the effects of vertical variation in the horizontal velocities may be neglected. This is a standard procedure in studies of both oscillatory and non-oscillatory flows (see, for example, Carrier and Greenspan, 1958; Roberts et al., 2000; Brocchini et al., 2001; Peregrine and Williams, 2001): it is known

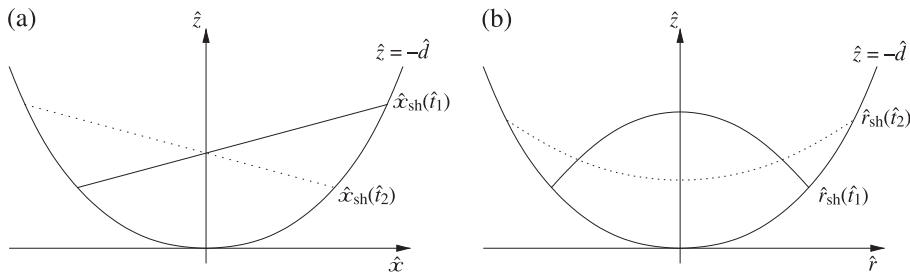


Fig. 1. Schematics (vertical scale exaggerated) showing cross sections of the basin with surface elevations at two points of the oscillation (solid and dotted lines): (a) axial mode (Section 3); (b) radial mode (Section 4).

to provide a good leading-order description of the hydrodynamics, in an analogous way to the von Kármán momentum integral approach to aerodynamic boundary layers (Batchelor, 1967).

The first correction to such a vertically uniform description of the flow would be to allow for the presence of a near-bed turbulent boundary layer, whose depth $\hat{\delta}$ scales with the maximum friction velocity \hat{u}_*^{\max} and the period of the motion,

$$\hat{\delta} \sim \frac{\hat{u}_*^{\max} \hat{T}}{2\pi}, \quad \text{where } \hat{u}_*^{\max} = \sqrt{\frac{\hat{\tau}_b^{\max}}{\hat{\rho}}} \quad (6)$$

for $\hat{\tau}_b^{\max}$, the maximum bed shear stress attained during an oscillation (Dyer, 1986). While we will not incorporate this correction in our description of the flow field, we will comment on its significance below.

A further dynamical simplification is the neglect of bed friction, which again follows studies such as Peregrine and Williams (2001). While this simplification has been applied successfully even in the swash zone, it is most valid in deeper water, away from the instantaneous shoreline; close to the shoreline, frictional effects may become important and may be modelled in a number of ways. For example, if we use the Chezy drag term, the frictional term omitted from Eqs. (4) and (5) has the dimensional magnitude $\hat{\tau}_d/\hat{h} = c_D \hat{\rho} |\bar{\mathbf{u}}|^2/\hat{h}$, where c_D is a dimensionless frictional coefficient which is typically of order 10^{-3} (Dyer, 1986). In dimensionless form, this term has the form $K|\mathbf{u}|^2/h$, where $K \equiv c_D \hat{D}x/\hat{D}_0$ is typically a small quantity. The region in which frictional terms are significant depends on the details of the hydrodynamics, and so the assumption that friction may be neglected will be discussed and justified a posteriori for each case considered.

2.2. Sediment dynamics

We describe the sediment dynamics in terms of the volumetric mass concentration of suspended sediment, $\hat{c}(\hat{x}, \hat{y}, \hat{z}, \hat{t})$. Defining the vertically averaged value

$$\bar{c}(\hat{x}, \hat{y}, \hat{t}) = \frac{1}{\hat{h}} \int_{-\hat{d}}^{\hat{h}-\hat{d}} \hat{c} d\hat{z}, \quad (7)$$

we may then construct a depth-averaged equation for the advective transport, erosion, and deposition of sediment,

$$\frac{\partial \bar{c}}{\partial \hat{t}} + \bar{u} \frac{\partial \bar{c}}{\partial \hat{x}} + \bar{v} \frac{\partial \bar{c}}{\partial \hat{y}} = \frac{1}{\hat{h}} [\hat{q}_e(\bar{u}, \bar{v}) - \hat{q}_d(\bar{u}, \bar{v}, \hat{c}_b)], \quad (8)$$

where \hat{q}_e and \hat{q}_d represent mass erosion and deposition rates, respectively, and \hat{c}_b is the near-bed suspended sediment concentration. These three quantities will be discussed in more detail below.

In constructing Eq. (8), we have neglected the turbulent diffusion of sediment in the horizontal plane, as the ratio of advective transport to turbulent diffusion scales as the ratio \hat{D}_x/\hat{D}_0 and so is typically much greater than unity. We have also used the approximation of vertical uniformity in the velocities, so that

$$\int_{-\hat{d}}^{\hat{h}-\hat{d}} \hat{\mathbf{u}} \hat{c} d\hat{z} = \bar{\mathbf{u}} \int_{-\hat{d}}^{\hat{h}-\hat{d}} \hat{c} d\hat{z} = \hat{h} \bar{\mathbf{u}} \bar{c}, \quad (9)$$

regardless of the precise vertical distribution of \hat{c} . Unlike the vertical distribution of velocity, the vertical distribution of suspended sediment may not necessarily be treated as uniform to first order and may vary in time.

It is helpful to define two dimensionless numbers. In a steady flow, the vertical distribution of suspended sediment arises from a balance between turbulent mixing and particle settling and may be described by the Rouse number $B \equiv \hat{w}_s/(\kappa \hat{u}_*)$, where \hat{w}_s is a particle settling velocity, $\hat{u}_* = \sqrt{\hat{\tau}_b/\hat{\rho}}$ is the friction velocity, which quantifies the turbulent intensity of the flow, and $\kappa \approx 0.4$ is the von Kármán constant. For Rouse numbers $B \ll 1$, the sediment may be treated as well-mixed in the water column, while for $B = \mathcal{O}(1)$, the vertical structure must be taken into account, and for $B \gg 1$, sediment concentrates in a near-bed boundary layer. The model which we employ for the vertical distribution of sediment is described below; for the moment, we note that in the current study, typical Rouse numbers will be in the range $B \lesssim 1$ (see Table 1), and so to leading order, we may neglect the rather complex dynamics of a near-bed boundary layer.

The second useful dimensionless number is a ‘bed exchange parameter’ $E_0 \equiv \hat{T}_0 \hat{w}_s/\hat{D}_0$. This describes the ratio of the time scale over which the fluid motion changes to the time taken for sediment to settle out of

Table 1

Approximate values of the governing dimensionless parameters for various values of the physical input quantities: cases correspond to those discussed in Section 3

Case	\hat{D}_s (m)	K	u_e	u_e/u_{\max}	E_0	B_0	η_b	C_b	E
(i)	10^{-4}	0.015	0.10	0.37	0.009	0.32	0.016	2.7	0.02
(ii)	3×10^{-4}	0.015	0.18	0.63	0.08	2.9	0.023	82	6.6
(iii)	3×10^{-5}	0.015	0.057	0.2	0.0008	0.03	0.011	1.12	0.0009
(iv)	2×10^{-4}	0.015	0.15	0.52	0.036	1.27	0.02	20.7	0.74

In each case, the maximum depth $\hat{D}_0 = 10$ m, the basin length $\hat{D}_x = 100$ m, and the dimensionless amplitude $A = 0.2$; consequently, the period is approximately 45 s and the boundary layer thickness is approximately 0.8 m (see text for discussion).

suspension; it can be thought of as a measure of how quickly the suspended sediment concentration adjusts to changes in the hydrodynamics.

It is also useful to express Eq. (8) in Lagrangian form. In this formulation, we follow fluid elements with position $\hat{\mathbf{x}}_L(\hat{t}; \hat{\mathbf{x}}_0)$, keeping track of the erosion and deposition which they experience, as well as of the changing vertical distribution of sediment within that fluid element. This is a natural way to view the sediment transport processes since suspended sediment is advected with the fluid.

The depth-averaged sediment concentration $\bar{c}_L(\hat{t})$ in a fluid element satisfies the equation

$$\frac{d}{d\hat{t}} \bar{c}_L(\hat{t}; \hat{\mathbf{x}}_0) = \frac{1}{\hat{h}_L} [\hat{q}_e(\bar{\mathbf{u}}_L) - \hat{q}_d(\bar{\mathbf{u}}_L, \hat{c}_{Lb})], \quad (10)$$

where the subscript L indicates that the variables are the Lagrangian quantities associated with a fluid element. The element position satisfies the advection equation

$$\frac{d\hat{\mathbf{x}}_L}{d\hat{t}} = \bar{\mathbf{u}}(\hat{\mathbf{x}}_L, \hat{t}). \quad (11)$$

The ordinary differential equation (10) is considerably more convenient to investigate analytically than the partial differential equation (8). In fact, as long as the deposition rate \hat{q}_d is linear in \bar{c}_L , Eq. (10) can be integrated analytically for any form of \hat{q}_e and \hat{q}_d , whenever the Lagrangian quantities $\hat{\mathbf{x}}_L$, $\bar{\mathbf{u}}_L$, and \hat{h}_L are known. This integration is described in greater detail in Appendix A.

Following Dyer and Soulsby (1988), we express \hat{c}_L in the form

$$\hat{c}_L = \bar{c}_L(\hat{t}) \mathcal{C}_L(\hat{z}, \hat{t}), \quad \text{where} \quad \int_{-\hat{d}}^{\hat{h}-\hat{d}} \mathcal{C}_L(\hat{z}, \hat{t}) d\hat{z} = \hat{h}. \quad (12)$$

Presuming the suspension is sufficiently dilute that there is no feedback effect of the suspended particles on the vertical distribution of turbulence, the ‘shape factor’ $\mathcal{C}(\hat{z}, \hat{t})$, which emerges from a balance between settling and mixing, depends only on the sediment properties and the leading-order (depth-averaged) hydrodynamics and is therefore a function of the Rouse number B , which is discussed further below.

The bed exchange fluxes \hat{q}_e and \hat{q}_d may be expressed in terms of the near-bed sediment concentration $\hat{c}_b = \bar{c} \mathcal{C}_b$, where \mathcal{C}_b is evaluated at a small reference height \hat{z}_b above the bed. This is in fact the only place in which the vertical distribution of \hat{c} enters our leading-order description of the sediment dynamics: we will show below how it can be absorbed into the bed exchange parameter E_0 .

We now consider the closures for the vertical distribution of suspended sediment and for the erosion and deposition rates.

2.2.1. Closures for the vertical structure

The simplest model of the vertical sediment distribution, which is formally valid in the regime $B \ll 1$, is to treat the sediment as being vertically well-mixed in the water column. In this case, $\mathcal{C} = 1$ and $\hat{c}_b = \bar{c}$.

More complex models of the vertical distribution involve specifying an eddy viscosity structure and solving the vertical equation for a balance between turbulent diffusion and settling. The available models vary widely in sophistication and tractability, and while their properties have been rather thoroughly investigated for steady flows (see, for example, Dyer and Soulsby, 1988), the nature of sediment response under oscillatory motions is rather less well understood.

In the current study, we follow the approach recently advocated by Soulsby (1997) and approxi-

mate the vertical distribution of sediment by a power-law profile (Dyer and Soulsby, 1988),

$$\hat{c}(\hat{\zeta}) = \hat{c}_b \left(\frac{\hat{z}_b}{\hat{\zeta}} \right)^{B_0} \quad \text{in } \hat{z}_b \leq \hat{\zeta} \leq \hat{h}. \quad (13)$$

Here, $\hat{\zeta} = \hat{z} + \hat{d}$ is the distance above the bed; B_0 is the ‘time-averaged’ Rouse number defined by $B_0 = \hat{w}_s / (\kappa \hat{u}^{*av})$, where $\hat{u}^{*av} = (\hat{\tau}^{av} / \hat{\rho})^{1/2}$ and $\hat{\tau}^{av}$ is the time-averaged bed shear stress over the period; and \hat{z}_b is the near-bed ‘reference height’ below which particles are considered to have settled out of the flow.

Integrating Eq. (13) from $\hat{\zeta} = \hat{z}_b$ to $\hat{\zeta} = \hat{h}$, we obtain the relation between the depth-averaged and near-bed concentrations,

$$\frac{\hat{c}_b}{\bar{c}} = \frac{1 - B_0}{\eta_b (\eta_b^{B_0 - 1} - 1)}, \quad (14)$$

where $\eta_b = \hat{z}_b / \hat{h}$. Values of both B_0 and η_b for our calculations are tabulated in Table 1, and the corresponding values of $\mathcal{C}_b = \hat{c}_b / \bar{c}$ are plotted in Fig. 2, which indicates that the variation of \hat{c} with depth can substantially increase the near-bed concentration (and thus the deposition rate) relative to a vertically well-mixed model.

To determine an appropriate value for \hat{z}_b , we follow the method due to van Rijn and described by Soulsby (1997), in which the reference height can be related to height of the mature bedforms which would occur under a unidirectional flow: the principal dependencies of \hat{z}_b are then that it increases with depth \hat{h} and

with particle size \hat{D}_s . We employ a simplified form of the van Rijn formula,

$$\eta_b = \frac{\hat{z}_b}{\hat{h}} = 0.519 \left(\frac{\hat{D}_s}{\hat{D}_0} \right)^{0.3}, \quad (15)$$

noting that more complex expressions for \hat{z}_b could readily be incorporated within the analytical framework described below.

2.2.2. Closures for the erosion and deposition rates

A wide range of empirical and semi-empirical expressions have been proposed to describe the entrainment and deposition of sediment, and none has as yet gained universal acceptance. In this study, we consider erosion rates of the form

$$\hat{q}_e(\bar{\mathbf{u}}) = \begin{cases} \hat{m}_e \left(\frac{|\bar{\mathbf{u}}|^2}{\hat{u}_e^2} - 1 \right)^n & \text{when } |\bar{\mathbf{u}}| > \hat{u}_e \\ 0 & \text{when } |\bar{\mathbf{u}}| \leq \hat{u}_e. \end{cases} \quad (16)$$

Here, \hat{m}_e is a dimensional erosion rate, \hat{u}_e is a critical velocity for the entrainment of sediment, which may be obtained from a Shields criterion (Dyer and Soulsby, 1988) together with the Chezy closure for bottom drag, and n is a dimensionless exponent. The prototypical sediment considered here will be in the grain size range 3×10^{-5} m (medium silt) to 3×10^{-4} m (fine sand), for which many of the models which have been employed in the literature have a more complicated form than that presented here (see, for example, the review by Garcia and Parker, 1991).

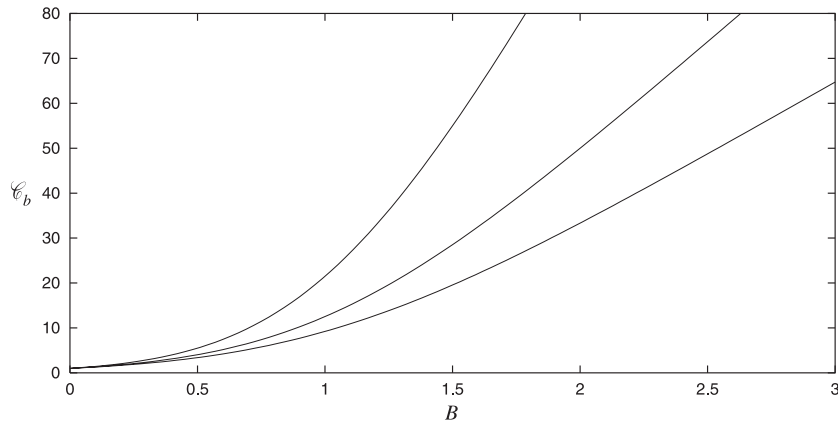


Fig. 2. The ratio between near-bed and depth-averaged sediment concentrations for various values of the Rouse number B_0 and for $\eta_b = 0.01$ (top line), 0.02, 0.03 (bottom line).

However, Eq. (16) shares the principal features of almost all such models, which are the existence of a critical shear stress for the entrainment of sediment and the asymptotic form $q_e \sim \tau_d^n$ for large bed stresses. By considering a range of values for n , we will demonstrate that the results obtained here are rather robust to the functional form of the erosional relation.

We also note that, with $n=1$ and appropriate choices for \hat{u}_e and \hat{m}_e , Eq. (16) may also be employed to describe the erosion of cohesive sediment (Dyer, 1986; Sanford and Maa, 2001).

We assume that particles are deposited with a constant settling velocity \hat{w}_s . In this case, the mass settling rate has the form

$$\hat{q}_d(\hat{c}_b) = \hat{w}_s \hat{c}_b = \hat{w}_s \bar{c}_b(\eta_b, B_0). \quad (17)$$

For the deposition of cohesive sediments which flocculate in the water column, more complicated deposition formulae such as that due to Einstein and Krone (1962) are commonly employed: Appendix A explains how these may be treated within the framework described here.

2.2.3. Nondimensionalisation

In nondimensionalising Eq. (8), we employ a concentration scale given by an order-of-magnitude balance between erosion and deposition, $\hat{c}_0 = \hat{m}_e / (\hat{w}_s \bar{c}_b)$, along with the hydrodynamic scales described earlier. We then obtain the nondimensional equation

$$\frac{\partial c}{\partial t} + \mathbf{u} \frac{\partial c}{\partial x} + v \frac{\partial c}{\partial y} = \frac{E}{h} [q_e(u, v) - q_d(u, v, c)], \quad (18)$$

where $E = E_0 \bar{c}_b(\eta_b, B_0)$ and where the net bed exchange term has the nondimensional form

$$q_e - q_d = \begin{cases} \left(\frac{|\mathbf{u}|^2}{u_e^2} - 1 \right)^n - c & \text{when } |\mathbf{u}| > u_e, \\ -c & \text{when } |\mathbf{u}| \leq u_e. \end{cases} \quad (19)$$

The Lagrangian form of Eq. (18) is

$$\frac{d}{dt} c_L(t; \mathbf{x}_0) = \frac{E}{h_L} [q_e(\mathbf{u}_L) - q_d(\mathbf{u}_L, c_L, t)],$$

where $\frac{d\mathbf{x}_L}{dt} = \mathbf{u}(\mathbf{x}_L, t)$. (20)

2.3. Summary of parameters and reference values

We now summarise the dimensionless parameters in this flow and calculate the values they take in particular situations. While the analysis will be presented in terms of dimensionless variables, we also provide dimensional examples of the predicted patterns of sediment movement.

The key dimensional parameters in these flows are the dimensions of the basin, \hat{D}_x and \hat{D}_0 , and the size of the sedimentary grains, \hat{D}_s . In addition, it is necessary to specify the mass erosion rate \hat{m}_e or, equivalently, the reference concentration \hat{c}_0 , which measures the magnitude of the suspended load. The period of the motion, \hat{T} , is determined by the dimensions of the basin, and anticipating subsequent sections, we find that $\hat{T} = \pi\sqrt{2}\hat{T}_0$, while the maximum dimensional velocity $\hat{u}_{\max} = A\sqrt{2}\hat{D}_x/\hat{T}_0$, where A is the amplitude of the motion (assumed to be less than unity).

Other important dimensional scales are determined as follows. Firstly, the bed shear stress is estimated using a Chezy drag law, $\hat{\tau}_b = c_D \hat{\rho} |\bar{\mathbf{u}}|^2$, and so the friction velocity $\hat{u}_* = |\bar{\mathbf{u}}| \sqrt{c_D}$. The settling velocity is estimated using Stokes' law,

$$\hat{w}_s = \frac{1}{18} \frac{\hat{\rho}_s - \hat{\rho}}{\hat{\mu}} \hat{g} \hat{D}_s^2, \quad (21)$$

which is appropriate for the low particle Reynolds numbers considered here. Finally, the critical velocity for erosion and suspension \hat{u}_e is estimated by setting the Shields parameter equal to unity. Thus, we find

$$\frac{\hat{\tau}_e}{\hat{g}(\hat{\rho}_s - \hat{\rho})\hat{D}_s} = 1 \quad \text{and so} \quad \hat{u}_e = \left[\frac{\hat{g}}{c_D} \frac{\hat{\rho}_s - \hat{\rho}}{\hat{\rho}} \hat{D}_s \right]^{1/2}. \quad (22)$$

Given these estimates of dimensional quantities, we now summarise the dimensionless parameters in the flow. These are the dimensional drag coefficient

$$K = c_D \frac{\hat{D}_x}{\hat{D}_0}; \quad (23)$$

the dimensionless critical velocity for erosion

$$u_e = \frac{1}{(\hat{g}\hat{D}_0)^{1/2}} \left[\frac{\hat{g}}{c_D} \frac{\hat{\rho}_s - \hat{\rho}}{\hat{\rho}} \hat{D}_s \right]^{1/2} \\ = \left[\frac{\hat{\rho}_s - \hat{\rho}}{c_D \hat{\rho}} \right]^{1/2} \left(\frac{\hat{D}_s}{\hat{D}_0} \right)^{1/2}; \quad (24)$$

the dimensionless bed exchange ratio

$$E_0 = \frac{\hat{T}_0 \hat{w}_s}{\hat{D}_0} = \frac{1}{18} \frac{\hat{\rho}_s - \hat{\rho}}{\hat{\mu}} \hat{g}^{1/2} \frac{\hat{D}_s^2 \hat{D}_x}{\hat{D}_0^{3/2}}; \quad (25)$$

and the Rouse number

$$B_0 = \frac{1}{18} \frac{\hat{\rho}_s - \hat{\rho}}{\hat{\mu}} \hat{g}^{1/2} \frac{1}{c_D \kappa} \frac{\hat{D}_s^2}{\hat{D}_0^{1/2}}. \quad (26)$$

To provide numerical estimates of these parameters, we assume the following standard values: $c_D = 1.5 \times 10^{-3}$ for a sandy to silty bed (Dyer, 1986), $\rho_s = 2.6 \times 10^3 \text{ kg m}^{-3}$ (Allen, 1985), $\kappa = 0.4$ (Dyer, 1986), $\mu = 10^{-3} \text{ kg m}^{-1} \text{ s}^{-1}$, and $\hat{g} = 10 \text{ m s}^{-2}$.

Table 1 provides approximate values of these quantities for a range of physically realistic conditions under seiche flow. We reiterate that the analysis and the discussion of results which follow are independent of the precise values taken by these parameters, although to relate the results to a particular physical example, these values must be specified.

Considering the values in Table 1, we find that the drag coefficient K is small for all cases, so we may expect the effects of friction to be confined to a small region close to the shoreline: this is discussed in more detail in Appendix B.

The typical Rouse numbers for fine sand and silt are of order 1, and so the near-bed suspended sediment concentration is generally substantially greater than the depth-averaged concentration, reducing the sediment response time and thus reducing lag effects. The bed exchange rate E , which quantifies how quickly the suspended sediment concentration responds to changes in the fluid velocity, is strongly dependent on sediment size, ranging from much smaller than 1 for fine silt (when we may expect considerable lags to occur) to rather greater than 1 for fine sand, for which lag effects may be less pronounced.

As a reference case, we will consider the values in the top row of Table 1, which correspond to silty sediment in a small lake or harbour. We will consider variation in the principal governing parameters about this value and discuss the robustness of our results to this variation.

Finally, we note briefly the values of two important dimensional quantities. The typical period of motions is of the order of a minute, which reflects the relatively small size of the basins considered here. The thickness of the oscillatory boundary layer $\hat{\delta}$, which may be calculated from Eq. (6), is a little less than a metre (i.e. around 10% of the water column). For fine sediment ($\hat{D}_s \leq 10^{-4} \text{ m}$), it is therefore generally less than the depth of the significantly sediment-laden region of the water column. For coarser sediment, it is possible that the inclusion of this boundary layer might modify our results somewhat; however, this lies beyond the scope of the current study.

2.4. Sediment fluxes and equilibrium concentrations

In order to interpret the results, it is useful to define two ‘equilibrium’ values of sediment concentration for a fluid element. The first is the instantaneous equilibrium value c_{eq} which arises from a balance between erosion and deposition,

$$c_{\text{eq}} = \begin{cases} \left(\frac{|\mathbf{u}|^2}{u_c^2} - 1 \right)^n & \text{when } |\mathbf{u}| > u_e, \\ 0 & \text{when } |\mathbf{u}| \leq u_e. \end{cases} \quad (27)$$

At a given instant, this value is the one towards which the concentration in a fluid element is adjusting, with the rate of adjustment proportional to the parameter E and inversely proportional to the depth of water h ; hence, in very shallow water near the shoreline, c_{eq} provides a good approximation to c and thus allows the concentration field to be determined.

The second ‘equilibrium’ quantity is that which arises from a balance between the net deposition and erosion over a period,

$$c_T = \frac{1}{T} \int_0^T \left(\frac{|\mathbf{u}_L(t)|^2}{u_c^2} - 1 \right)^n dt, \quad (28)$$

where T is the period of the oscillation. This constant value provides a good approximation to c in deep water, where the sediment load responds only very slowly to changes in $|\mathbf{u}|$.

To assess the morphodynamic effect of the sediment transport described here, we calculate the net sediment flux over a period of the fluid motion. The instantaneous flux $\mathbf{q}(x, y, t)$ is defined as

$$\mathbf{q}(x, y, t) = \int_{-d}^{h-d} c(x, y, z, t) \mathbf{u}(x, y, z, t) dz, \quad (29)$$

which to leading order in the vertical velocity structure is equal to $ch\mathbf{u}$, regardless of the vertical sediment concentration distribution $\mathcal{C}(z)$. The net flux over a period is then given by

$$\mathbf{Q}(x, y) = \int_0^T \mathbf{q}(x, y, t) dt, \quad (30)$$

where T is the period of the motion and the net mass of sediment deposited at a point over one period of the motion is given by $M(x, y) = -\nabla \cdot \mathbf{Q}$.

For the radial flows discussed in Section 4, we have $\mathbf{u} = u_r(r, z, t) \mathbf{e}_r$, where $r^2 = x^2 + y^2$ and \mathbf{e}_r is the unit vector in the radial direction. We then have $\mathbf{q} = cu_r h \mathbf{e}_r$, and it follows that $\mathbf{Q}(r) = Q(r) \mathbf{e}_r$, where

$$Q(r) = \int_0^T q(r, t) dt, \quad \text{and so} \\ M(r) = -\frac{1}{r} \frac{d}{dr} \left(r \frac{dQ}{dr} \right). \quad (31)$$

It is useful to consider these quantities in dimensional terms. If the seiching persists for a time \hat{T}_{sei} , then the net depth of erosion at a point over that time is given by

$$\hat{Z}_e = \frac{\hat{T}_{\text{sei}}}{\hat{T}} \frac{\hat{c}_0}{\hat{c}_{\text{bed}}} \hat{D}_0 M, \quad (32)$$

where \hat{c}_{bed} is the mass concentration of particles in the bed, which for a packing fraction of around 0.7 is approximately 1800 kg m^{-3} , and where \hat{c}_0 is the reference concentration defined above. We will employ this formula in subsequent sections to quantify the morphological importance of these flows: for this purpose, we will take \hat{c}_0 to be defined such that the long-term average concentration \hat{c}_T in the most rapidly

moving fluid element is of the order of 1 kg m^{-3} , and we will quote the results for a seiching time of 1 hour.

3. Axial flow in an elliptical basin

We now describe the two principal modes of oscillation obtained by Thacker (1981), and we calculate the resulting sediment transport. In this section, we consider unidirectional flow parallel to one axis of the basin, and in the next section, we consider radial flow.

3.1. Hydrodynamics

Thacker (1981) obtained solutions for various modes of flow in which the free surface is planar (Fig. 1a). We consider the simplest such mode: this describes flow in an elliptical basin, $d(x, Y) = 1 - x^2 - Y^2$, where, for notational convenience, we have defined the rescaled lateral coordinate $Y = \hat{y} / \hat{D}_y$. The solutions are such that the oscillatory flow is parallel to one axis of the ellipse, and without loss of generality, we take this to be the x -axis, $\mathbf{u} = (u, 0)$.

Thacker's solutions have the form

$$u(t) = -A \cos \omega t, \quad v = 0, \quad \text{and} \\ h(x, y, t) = 2A \cos \omega t \left(x - \frac{A}{2} \cos \omega t \right) + (1 - x^2 - Y^2), \quad (33)$$

where A represents a dimensionless amplitude for the motion and where $\omega = \sqrt{2}$. The amplitude A may take any value, but for physically plausible seiching motions, we consider rather small values of A . It may be verified by direct substitution that Eq. (33) do indeed satisfy the shallow-water equations (3), (4) and (5).

It is simple to obtain the Lagrangian description,

$$x_L(t; x_0) = x_0 - A + A \cos \omega t, \\ u_L(t) = -A \omega \sin \omega t \quad \text{and} \\ h_L(x_0, Y) = 1 - R^2, \quad \text{where } R^2 = (x_0 - A)^2 + Y^2, \quad (34)$$

and where x_0 is the original x -coordinate of the fluid element. The depth of fluid is known in terms of the

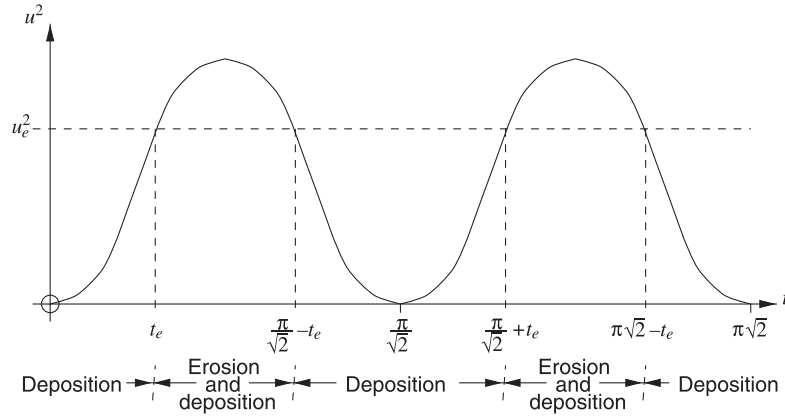


Fig. 3. Schematic illustrating the magnitude of u^2 as a function of time, and the corresponding intervals of simultaneous erosion/deposition and of pure deposition. These are used to construct the Lagrangian concentration field.

single quantity R , and so we immediately obtain the result that, at any instant in time, concentration c must be constant on the ellipses $R^2 = (x - A \cos \omega t)^2 + Y^2 = \text{constant}$. (The shoreline $h=0$ is a special case of these curves, with $R = \pm 1$, and is given by $x_{\text{sh}} = \sqrt{1 - Y^2} + A \cos \omega t$.) We also note that the forcing in the Lagrangian equation (10) has period $\pi/\sqrt{2}$, half that of the Eulerian motion, and so we seek a Lagrangian solution $c_L(t; R)$ which shares this periodicity (although after substituting in for $R(x, y, t)$, the Eulerian solution will have period $\pi\sqrt{2}$).

3.2. Construction of the solution

We now sketch the construction of the solution; more complete mathematical details can be found in Appendix A. The solution is constructed by dividing the period of a fluid oscillation into successive intervals in which $|\mathbf{u}| > u_e$ and $|\mathbf{u}| < u_e$. In each such interval, the Lagrangian concentration Eq. (10) may be solved explicitly for each fluid element, given the initial concentration, and the concentration at the end of that (erosional or depositional) interval is then used to set the concentration at the start of the succeeding (depositional or erosional) interval. Finally, by identifying the concentration at the end of a period with that at the start, we obtain a periodic solution for $c_L(t)$ in each fluid element.

It is helpful to refer to Fig. 3, which shows the successive erosional and depositional intervals experienced by a given fluid element.

The starts and ends of these intervals are given by the times $t_0 = t_e$, $t_1 = \pi/\sqrt{2} - t_e$, $t_2 = \pi/\sqrt{2} + t_e$, and so forth, where t_e is such that $|u_L(t_e)| = u_e$, i.e.

$$t_e = \frac{1}{\sqrt{2}} \sin^{-1} \left(\frac{u_e}{\sqrt{2}A} \right). \quad (35)$$

During erosional intervals, when $|u_L| > u_e$, the concentration equation (10) has the form

$$\frac{dc_L}{dt} = \frac{E}{h_L} \left[\left(\frac{u_L^2}{u_e^2} - 1 \right) - c_L \right] \equiv a_e(t) - c_L(t)b_e(t), \quad (36)$$

and the solution has the form $c_L(t) = \Theta_e(t, t_k) + c_k \Omega_e(t, t_k)$, where $t = t_k$ is the start of the interval, c_k is the concentration at $t = t_k$, and the quantities Ω_e and Θ_e are defined as

$$\Omega_e(t, t_k) = \exp \left[-\frac{E(t - t_k)}{1 - R^2} \right] \quad (37)$$

and

$$\Theta_e(t, t_k) = \exp \left[-\frac{E(t - t_k)}{1 - R^2} \right] \int_{t_k}^t \exp \left[\frac{E(\tau - t_k)}{1 - R^2} \right] \times \frac{E}{1 - R^2} \left[\frac{2A^2 \sin \omega \tau}{u_e^2} - 1 \right]^n d\tau. \quad (38)$$

During depositional intervals, when $|u| < u_c$, Eq. (10) has the form

$$\frac{dc_L}{dt} = -\frac{E}{h_L}c_L = -b_d(t)c_L(t), \quad (39)$$

and the solutions can be expressed as $c_L = c_k \Omega_d(t, t_k)$, where t_k and c_k are defined as before and where $\Omega_d(t, t_k) = \Omega_e(t, t_k)$. The quantities $\Omega_e(t, t_k)$ and $\Omega_d(t, t_k)$ quantify the exponential decay of the concentration field as particles settle out during periods of low current speed, while $\Theta_e(t, t_k)$ quantifies the effect of simultaneous erosion and deposition while $|u| > u_c$. The integral for Θ_e may be evaluated in terms of elementary functions when n is a positive integer and is relatively simple to compute for noninteger n .

Finally, having constructed our periodic solution for $c_L(t; R)$, we substitute for $R^2 = (x - A \cos \omega t)^2 + Y^2$ to obtain the Eulerian solution $c(x, Y, t)$.

3.3. Typical solutions

In principle, we may vary the dimensionless parameters of the model independently and thus investigate questions such as the dependence of the solutions on the critical Shields parameter or their sensitivity to the sediment entrainment and deposition models in con-

siderable detail. Our main interest here is in illustrating the basic processes, and so we will select a representative ‘reference case’ (case (i) in Table 1) and discuss it in some detail first. We will briefly consider the robustness of this result to small changes in the parameters, but the main form of variation we are interested in occurs as the sediment size \hat{D}_s is varied leaving all other physical parameters unchanged. This is an important variation for two reasons. Firstly, we may expect a range of sediment sizes in any physical context, and it is important to be aware of the different behaviour which may be expected from different sediment modes. Secondly, the scalings in Section 2.3 indicate that the effective bed exchange parameter E varies very strongly with \hat{D}_s , both through the direct variation $\hat{w}_s \propto \hat{D}_s^2$ and through the tendency of larger particles to be transported closer to the bed, as $B_0 \propto \hat{D}_s^2$. Consequently, a single decade of variation in \hat{D}_s leads to almost four decades of variation in E (see Table 1) and may thus lead to important differences in the lag-driven net transport patterns.

3.3.1. Reference case (i)

Fig. 4 shows the concentration field for $Y=0$, in other words, along the centreline of the ellipse. Only the region $x > 0$ is plotted, as the rest may be obtained

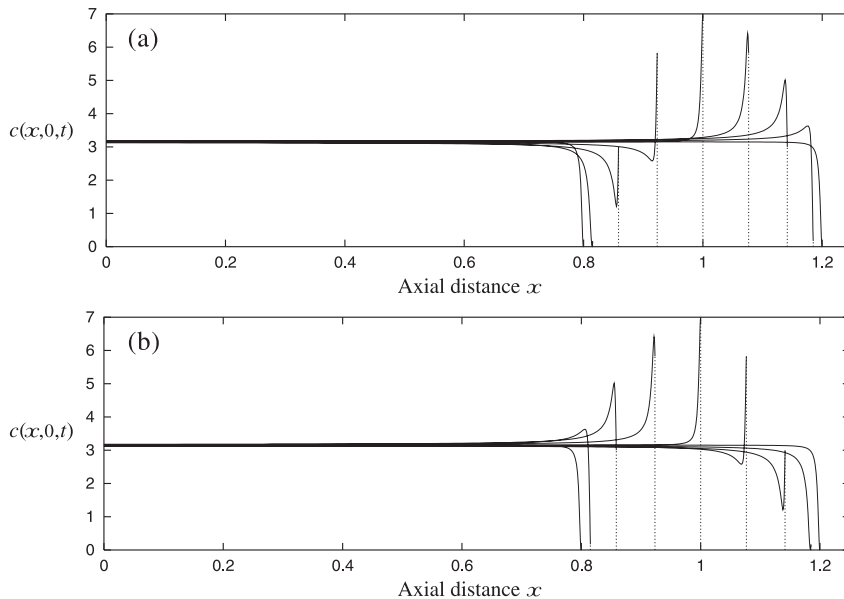


Fig. 4. Analytical solution for suspended sediment concentration under axial flow, for reference case (i) with $n=1$. (a) On-shore flow; (b) offshore flow.

by symmetry, and plots for other values of Y are omitted as they share the same qualitative features as those for $Y=0$.

The most prominent feature of the solutions is the maximum of suspended sediment concentration which forms near or at the shoreline during erosive periods, and which is reminiscent of the ‘turbid edge’ which has been observed in tidal flow over mudflats (Christie and Dyer, 1998). Especially at the start of phases of onshore and offshore flow, when fluid accelerations are highest, the peak in c is very sharply defined and may be somewhat exaggerated by the neglect of friction in the hydrodynamics (see Appendix B). In contrast to the solution under radial flow which will be described in Section 4, velocities in the centre of the basin are sufficient to suspend sediment, and since it only settles out slowly, concentrations are maintained here throughout the oscillation. The main difference between concentrations at

the edge and in the centre of the basin is the greater variability of c over a cycle, which occurs because of the shallower water: otherwise, the dynamics are almost identical.

Although the solutions for the suspended sediment concentration field $c(x, y, t)$ are periodic in time, they may produce a net flux of sediment through the well-known processes of settling and scour lag (Dyer, 1986; Le Hir et al., 2000). Both processes refer to a hysteresis effect: because it takes a finite time (which is controlled by E and by the local depth of water h) for the concentration field to adjust to equilibrium with the local velocity field, the net fluxes of sediment in different directions do not necessarily cancel out over a period of the oscillation. It is usual to distinguish between settling lag, which refers to hysteresis associated with deposition, and scour lag, which refers to hysteresis associated with erosion (see for example Le Hir et al., 2000; Bartholdy, 2000); however, it is

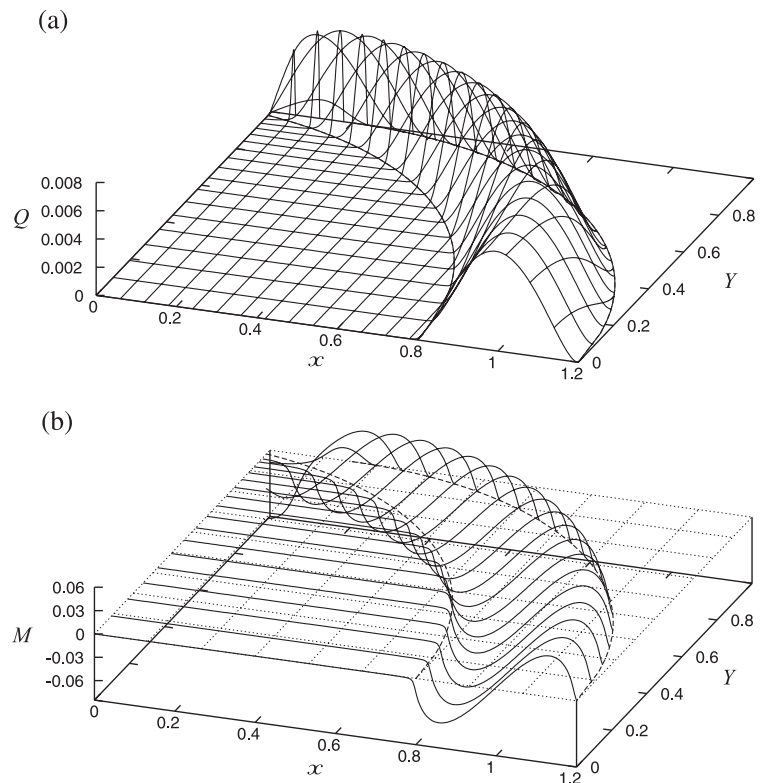


Fig. 5. Analytical solutions for (a) net flux Q over a period; (b) net deposition $M = -\partial Q/\partial x$ over a period under axial flow, for reference case (i) with $n = 1$. Dashed lines indicate the positions of the shoreline at maximum run-up and run-down; dotted grid indicates the surface $M=0$ (no net erosion or deposition).

not clear that in the current context, it is helpful to separate these processes, and so here and in subsequent sections, we refer to them together under the general term ‘suspension lag’.

We have recently given a rather more detailed discussion of the mechanisms of suspension lag for cohesive sediment (Pritchard and Hogg, submitted for publication (a)), and the same principles apply in the present case. Essentially, the lag associated with the deposition and re-entrainment of material seen in the Eulerian frame corresponds to the transfer of sediment between fluid parcels in the Lagrangian frame and thus to a net spatial movement of sediment. In many situations, the dominant effect of suspension lag under tidal flows is to transfer material landwards into the shallower regions of an estuary or inlet (Nichols and Biggs, 1985), and we observe (Fig. 5) that the same occurs here.

Fig. 5 illustrates the pattern of net cross-shore sediment flux $Q(x, Y)$ and the corresponding pattern of net erosion and deposition for our reference case. Only the region ($x > 0, Y > 0$) is shown since the rest can be obtained by symmetry.

The first interesting feature is that $Q > 0$ throughout the region $x > 0$, so the residual flux is always directed axially outwards. In other words, the effect of sus-

pension lag under this mode of oscillation is to move material shorewards, depositing it in the shallower part of the basin during the deposition period around maximum run-up.

The greatest net cross-shore fluxes occur in regions between the maximum and minimum extents of the shoreline, which are inundated during only part of the oscillation. This represents a balance between the enhancement of suspension lag effects in moderately shallow water, when the concentration changes significantly over a period, and the vanishing of the sediment load ch at the shoreline. By symmetry, there can be no net transport across the line $x = 0$, and in fact, there is a substantial region around $(x, Y) = (0, 0)$ in which Q is very low since concentrations do not vary greatly in deep water over the course of a period (Fig. 4). We also note that the net fluxes are rather small compared to the peak instantaneous fluxes q , which are of order 1: thus, the imbalance between seaward and landwards fluxes which leads to net transport is a rather delicate one.

Fig. 5b illustrates the net erosion and deposition due to a single seiche: material is eroded from a region just landwards of the position of maximum run-down and deposited just seawards of the position of maximum run-up. Employing the approach described in

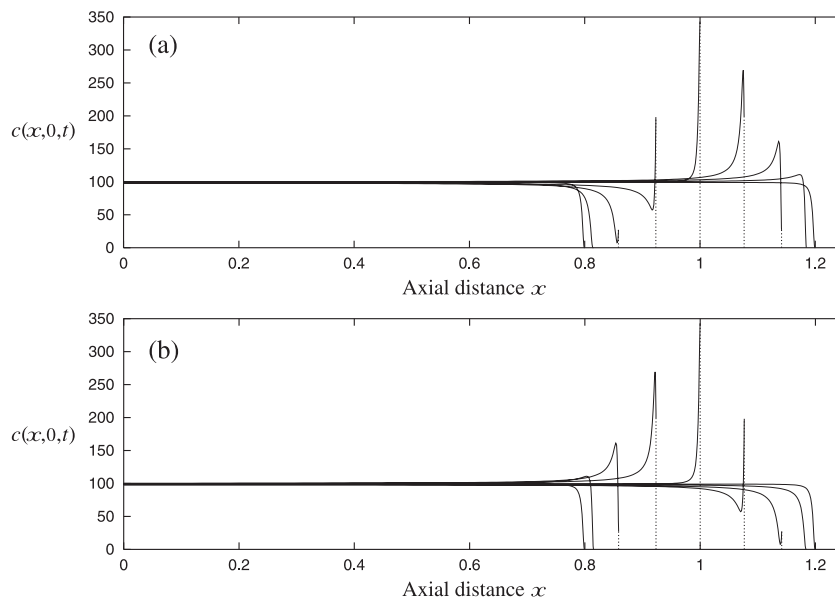


Fig. 6. Analytical solution for suspended sediment concentration under axial flow, for reference case (i) with $n = 3$. (a) On-shore flow; (b) offshore flow.

Section 2.4 to obtain the net erosion and deposition in dimensional terms, we find that the maximum bed level change represented in Fig. 5b is $|\hat{Z}_c| \approx 8$ mm over 1 hour of seiching.

3.3.2. Robustness of the reference case (i)

We now briefly describe the robustness of the solution for the reference case (i) to small changes in the dimensionless parameters. Variations in E will be dealt with in the next section; we consider variations in the erosion exponent n , in the dimensionless erosion velocity u_c , and in the dimensionless amplitude of the seiching motion A .

Figs. 6 and 7 illustrate the effect of varying the exponent n in the erosion formula from 1 to 3. The immediately obvious effect of taking a higher value of n is to increase the average concentration of suspended sediment by a factor of about 30 and the peak concentration by a factor of about 50: the dimension-

less net flux increases in proportion to this. (This increase, however, is largely an artefact of the non-dimensionalisation selected: we recall that the concentration scale is proportional to the dimensional parameter \hat{m}_c , and there is no reason why this should have the same value for different values of n . Recall that in calculating the net bed level changes $|\hat{Z}_c|$, we normalise by \hat{c}_T .)

Perhaps surprisingly, there is almost no qualitative difference between the solutions for different values of n . For $n=3$, erosion is slightly slower than for $n=1$ when $u^2 - u_c^2$ is small, and conversely more rapid when u^2 is greater, and this shows up in the plots of c , where the peak value of c_{eq} is increased somewhat more than the value c_T in deeper water. It is also evident in the slightly slower growth of the shoreline concentration maximum and in the generally slightly higher variation of the concentration field in shallow water. As Fig. 7 illustrates, however,

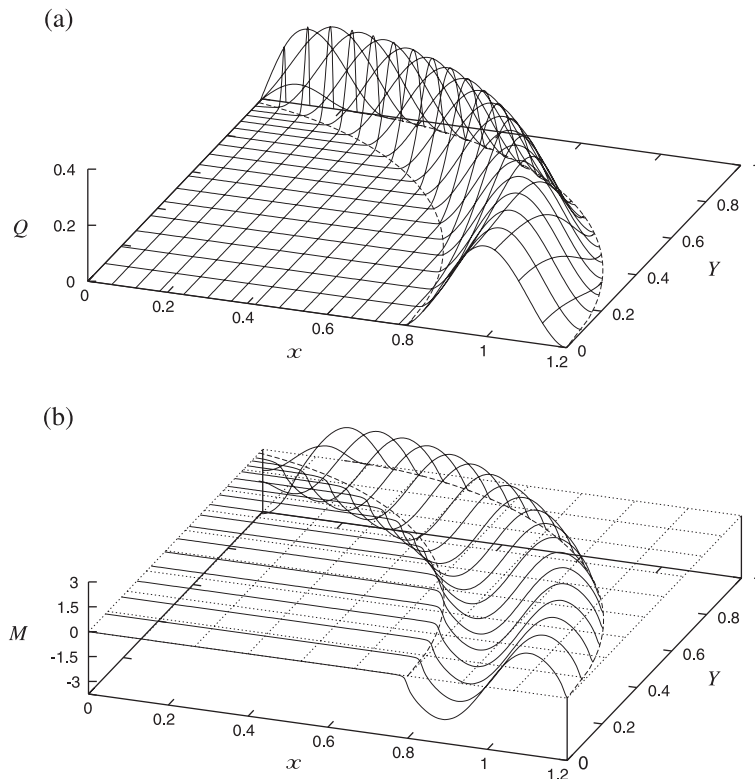


Fig. 7. Analytical solutions for (a) net flux Q over a period; (b) net deposition $M = -\partial Q/\partial x$ over a period under axial flow, for reference case (i) with $n=3$. Dashed lines indicate the positions of the shoreline at maximum run-up and run-down; dotted grid indicates the surface $M=0$ (no net erosion or deposition). The maximum bed level change in dimensional variables is $|\hat{Z}_c| \approx 1.3$ cm over an hour of seiching.

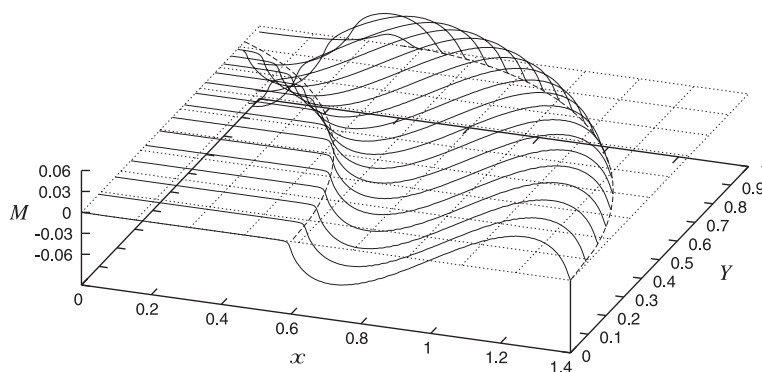


Fig. 8. Analytical solution net deposition $M = -\partial Q/\partial x$ over a period under axial flow, for reference case (i) with $n=1$ and the revised values $A=0.4$, $u_c=0.2$. Dashed lines indicate the positions of the shoreline at maximum run-up and run-down; dotted grid indicates the surface $M=0$ (no net erosion or deposition). The maximum bed level change in dimensional variables is $|\hat{Z}_c| \approx 8$ mm over an hour of seiching.

these features have very little influence on the pattern of net sediment transport across the basin; and in fact, the maximum bed level change \hat{Z}_c is

increased by a factor of less than 2, reflecting the slightly enhanced lag effects which occur for higher values of n .

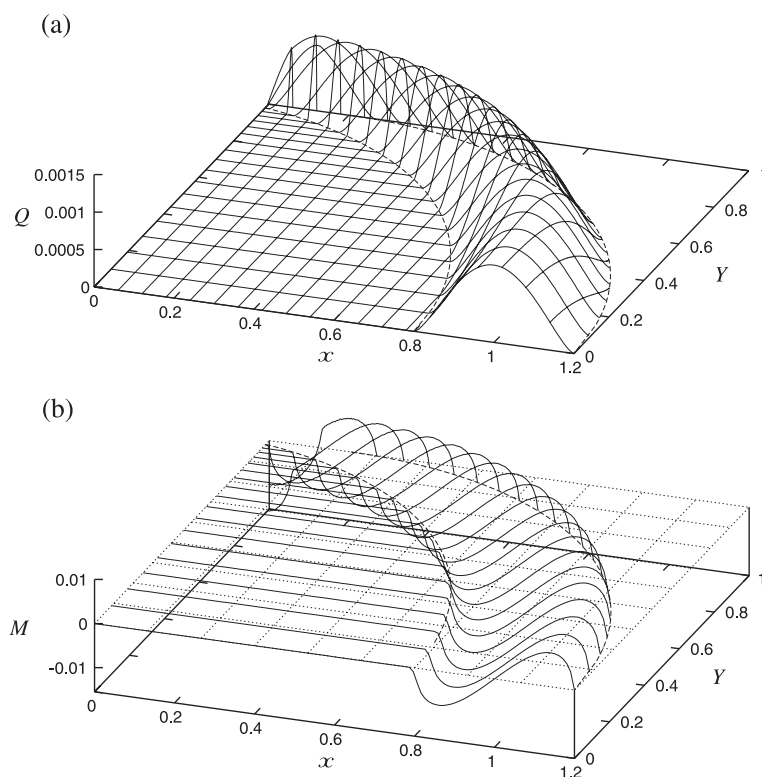


Fig. 9. Analytical solutions for (a) net flux Q over a period; (b) net deposition $M = -\partial Q/\partial x$ over a period under axial flow, for case (iii) with $n=1$. Dashed lines indicate the positions of the shoreline at maximum run-up and run-down; dotted grid indicates the surface $M=0$ (no net erosion or deposition). The maximum bed level change in dimensional variables is $|\hat{Z}_c| \approx 1.3$ mm over an hour of seiching.

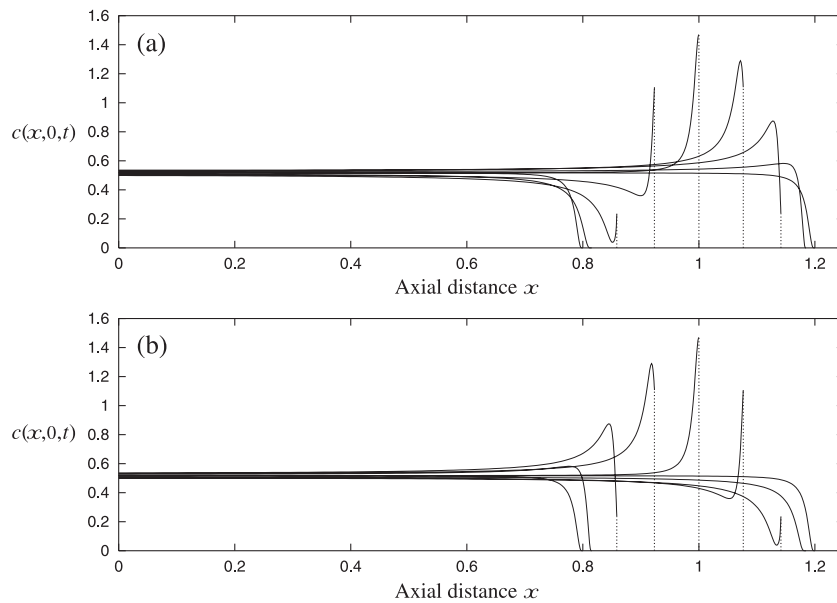


Fig. 10. Analytical solution for suspended sediment concentration under axial flow, for case (ii) with $n=1$. (a) On-shore flow; (b) off-shore flow.

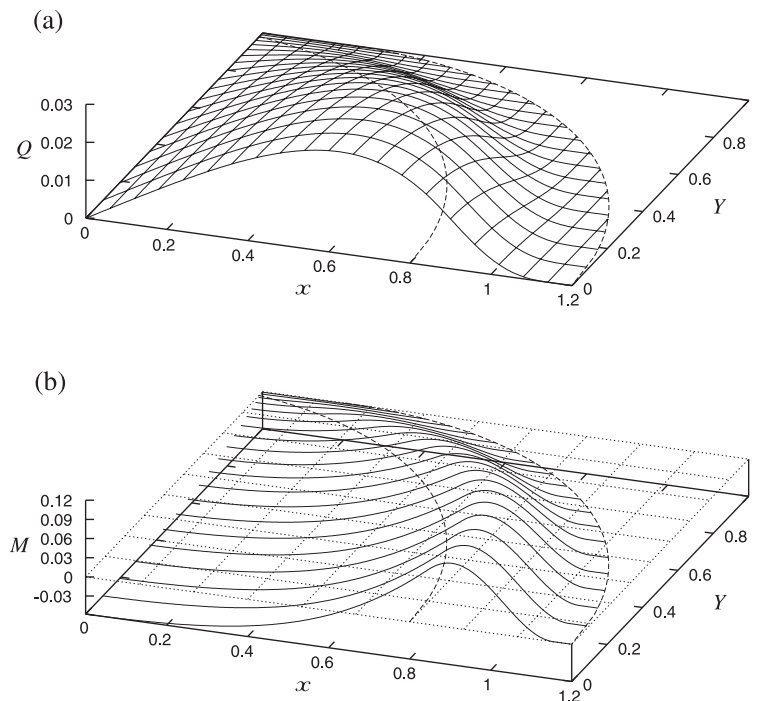


Fig. 11. Analytical solutions for (a) net flux Q over a period; (b) net deposition $M = -\partial Q / \partial x$ over a period under axial flow, for case (ii) with $n=1$. Dashed lines indicate the positions of the shoreline at maximum run-up and run-down; dotted grid indicates the surface $M=0$ (no net erosion or deposition). The maximum bed level change in dimensional variables is $|\hat{Z}_c| \approx 1.6$ cm over an hour of seiching.

Varying the dimensionless erosion velocity u_e has the effect which might be expected: as u_e decreases, concentrations generally increase and so, therefore, do the net fluxes. The pattern of transport, however, is unaltered, and so the plots are omitted for brevity. Increasing u_e from 0.1 to 0.15 reduces \hat{Z}_e to approximately half its value, while decreasing u_e from 0.1 to 0.05 increases \hat{Z}_e by a factor of almost 5. (To leading order, we can estimate these changes by assuming that \hat{Z}_e is proportional to a ‘typical’ value of the erosion rate $q_e^{typ} = (u_{typ}^2/u_e^2 - 1)$; this may be a useful tool for adapting these calculations to obtain estimates of morphological change without recalculating the solutions.)

Finally, varying the dimensionless amplitude A while keeping the ratio u_e/u_{max} constant has almost no effect on the maximum bed level change, and the pattern of erosion and deposition relative to the shoreline positions remains effectively the same (Fig. 8).

3.3.3. Effect of varying the particle size

As noted above, altering the particle size \hat{D}_s has a very strong effect on the effective bed exchange

parameter $E = \hat{w}_s \mathcal{C}_b \hat{T} / \hat{D}_0$. This quantifies how rapidly the concentration responds to changes in the fluid velocity and, consequently, may be expected to modify the suspension lag effects which lead to the net sediment transport patterns discussed above.

Fig. 9 illustrates the effect on transport patterns of reducing the sediment grain size from 0.1 to 0.03 mm (i.e. from coarse to fine silt): the parameter values are given as case (iii) in Table 1. As for the reference case (i), transport is effectively confined to the region between maximum run-up and run-down of the shoreline. This is because we are still in the regime $E \ll 1$, and so it is only in very shallow water $h \sim E$ where significant changes to the suspended sediment concentration may occur in the course of an oscillation.

It is more interesting to consider the effect of increasing the grain size. The concentration field and net transport patterns for $\hat{D}_s = 0.3$ mm (case (ii) in Table 1) are shown in Figs. 10 and 11, respectively, while the transport patterns for the intermediate value $\hat{D}_s = 0.2$ mm (case (iv) in Table 1) are shown in Fig. 12.

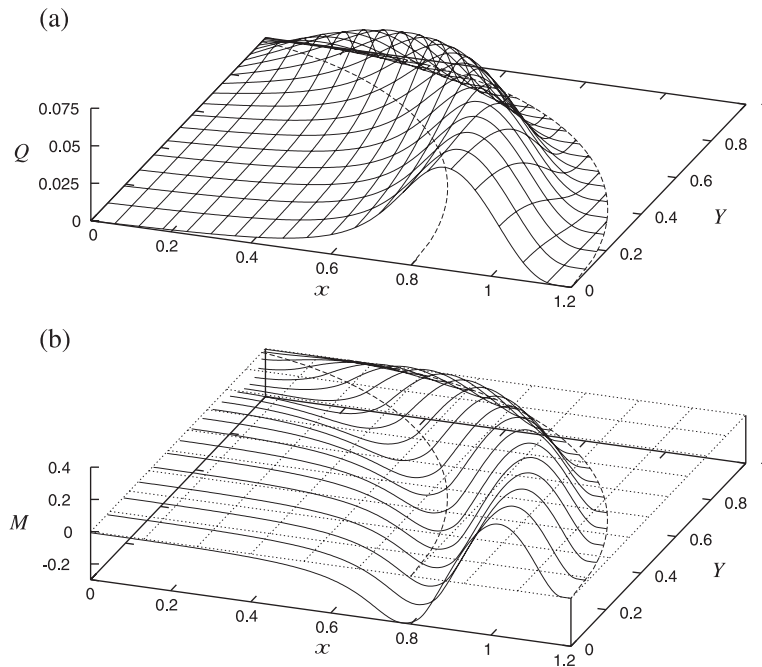


Fig. 12. Analytical solutions for (a) net flux Q over a period; (b) net deposition $M = -\partial Q / \partial x$ over a period under axial flow, for case (iv) with $n = 1$. Dashed lines indicate the positions of the shoreline at maximum run-up and run-down; dotted grid indicates the surface $M = 0$ (no net erosion or deposition). The maximum bed level change in dimensional variables is $|\hat{Z}_e| \approx 5.4$ cm over an hour of seiching.

The considerably larger value of E for case (ii) leads to a much more substantial variation of suspended sediment concentration over the course of a cycle: there is even a noticeable variation in the deepest water in the centre of the basin (Fig. 10). This means that suspension lag is effective throughout the basin, and, in fact, it is now least evident in very shallow water (note the decay of Q towards the position of maximum run-up in Fig. 11a).

Because suspension lag now occurs preferentially in rather deeper water, the transport pattern in general is shifted towards the centre of the basin. The region of net deposition now encompasses everywhere between maximum run-up and run-down, as well as some distance seawards of this, while sediment is eroded throughout the interior of the basin. If similar patterns are able to occur for extended periods of time, the net effect will be to deepen the basin while forming a steeper ‘lip’ around its edge, ultimately reducing its lateral extent.

The greater effectiveness of suspension lag for coarser sediment also leads to distinctly higher rates of erosion and deposition, with \hat{Z}_c for case (ii) being some 10 times greater than for case (i). Case (ii), however, does not represent the maximum bed level change possible: this can be expected to occur when E is of order 1, allowing lag effects to occur in both the deeper and shallower parts of the basin.

This is illustrated in Fig. 12, which shows the transport patterns for case (iv). The overall pattern is intermediate between those for cases (i) and (ii), with the erosional region around maximum run-down still evident, but now with some net transport and erosion even in the centre of the basin. The rates of change here may be as high as several centimetres of deposition in an hour of seiching, suggesting that for sandy sediments, this may be a rather significant morphodynamical process.

4. Radial flow in a circular basin

4.1. Hydrodynamics and construction of the solution

In this section, we consider flows in a circular basin, $d(r) = 1 - r^2$, where $r^2 = x^2 + y^2$. In this bathymetry, modes of oscillation are possible in which the fluid motion is entirely in the radial

direction, $\mathbf{u} = u_r \mathbf{e}_r$, and the free surface is axisymmetric (Fig. 1b).

Thacker (1981) obtained solutions in which the free surface is a quadratic function of r . In dimensionless variables, Thacker’s solutions have the form

$$u_r(r, t) = \sqrt{2\alpha r} \frac{\sin\sqrt{8}t}{1 - \alpha\cos\sqrt{8}t} \quad (40)$$

and

$$h(r, t) = \left[\frac{\sqrt{1 - \alpha^2}}{1 - \alpha\cos\sqrt{8}t} - r^2 \left(\frac{1 - \alpha^2}{(1 - \alpha\cos\sqrt{8}t)^2} \right) \right], \quad (41)$$

where $\alpha < 1$ represents a dimensionless amplitude for the change in elevation at the centre of the basin (note that as $\alpha \rightarrow 1$, the motion becomes unbounded). For notational convenience, for the remainder of this section, we will write $u(r, t) = u_r(r, t)$.

Fluid elements then have position $r_L(t; r_0)$, radial velocity $u_L(t; r_0)$, and depth $h_L(t; r_0)$ given by

$$\begin{aligned} r_L(t; r_0) &= \frac{r_0}{\sqrt{1 - \alpha}} \sqrt{1 - \alpha\cos\sqrt{8}t}, \\ u_L(t; r_0) &= \frac{\sqrt{2\alpha r_0}}{\sqrt{1 - \alpha}} \frac{\sin\sqrt{8}t}{\sqrt{1 - \alpha\cos\sqrt{8}t}}, \\ h_L(t; r_0) &= \frac{\sqrt{1 - \alpha^2} - r_0^2(1 + \alpha)}{1 - \alpha\cos\sqrt{8}t}. \end{aligned} \quad (42)$$

We note that $t=0$ corresponds to the innermost position of a fluid element.

The shoreline occurs at $r = r_{sh}(t)$, where

$$r_{sh}(t) = r_L(t; r_{0sh}) \quad \text{for} \quad r_{0sh} = \left(\frac{1 - \alpha}{1 + \alpha} \right)^{1/4}. \quad (43)$$

The maximum velocity attained by the fluid element labelled by r_0 is

$$u_m(r_0) = 2r_0 \frac{\sqrt{1 - \sqrt{1 - \alpha^2}}}{\sqrt{1 - \alpha}}, \quad (44)$$

while the maximum and minimum radial positions of this element are

$$r_{\min}(r_0) = r_0 \quad \text{and} \quad r_{\max}(r_0) = r_0 \sqrt{\frac{1+\alpha}{1-\alpha}}. \quad (45)$$

Thus, we obtain the maximum velocity under an oscillation, which is given by

$$u_{\max} = u_m(r_{0\text{sh}}) = 2 \left(\frac{1 - \sqrt{1 - \alpha^2}}{\sqrt{1 - \alpha^2}} \right)^{1/2}. \quad (46)$$

If we require that the maximum velocity under this mode of seiching is equal to that under the axial flows considered in Section 3, it then follows that

$$\alpha = \sqrt{1 - \left(1 + \frac{A^2}{2}\right)^{-2}}, \quad (47)$$

so we may obtain flows which are ‘equivalent’ to the reference case (i) of Section 3 by setting $\alpha \approx 0.2$ and taking other parameter values as in Table 1.

Eq. (46) also provides a bound on the region of parameter space in which the seiche is morphodynamically effective: clearly, if $u_e \geq u_{\max}$, then no sediment transport can occur. When $u_e \leq u_{\max}$, then we may use the Lagrangian description to determine which region of the basin is morphodynamically active: this is given by $r > r_{0^*}(u_e)$, where $u_m(r_{0^*}) = u_e$. A little algebra reveals that

$$\begin{aligned} r_{0^*}(u_e) &= \frac{1}{2} u_e \frac{(1 - \alpha)^{1/2}}{(1 - \sqrt{1 - \alpha^2})^{1/2}} \\ &= \frac{u_e}{u_{\max}} \left(1 + \frac{u_{\max}^2}{4} - u_{\max} \sqrt{\frac{1}{2} + \frac{u_{\max}^2}{16}} \right)^{1/2}. \end{aligned} \quad (48)$$

Fig. 13 illustrates the variation of the morphodynamically active region with u_{\max} and u_e . It is apparent that for a fixed threshold of erosion u_e , as the amplitude of the motion is reduced, the region in which the sediment is mobilised is squeezed into a progressively narrower strip behind the shoreline.

The final quantities which we will require in the construction of the solution are the times at which the Lagrangian velocity u_L is equal to the critical value u_e .

It is helpful at this point to refer to Fig. 14, which illustrates the key features of the solution in the (r, t) plane: recall that the period of the motion is $\pi/\sqrt{2} \approx 2.22$. We define

$$t_{\pm}(u) = \frac{1}{\sqrt{8}} \cos^{-1} \left[\frac{1}{2\alpha} (k \pm \sqrt{k^2 - 4k + 4\alpha}) \right],$$

where $k = \frac{1 - \alpha}{2} \left(\frac{u}{r_0} \right)^2$, (49)

and we find that $u_L = u_e$ at the successive times $t_{e1} = t_+(u_e)$ and $t_{e2} = t_-(u_e)$, and then $u_L = -u_e$ at the further succeeding times $t_{e3} = \pi/\sqrt{2} - t_-(u_e)$ and $t_{e4} = \pi/\sqrt{2} - t_+(u_e)$.

We now construct periodic solutions using the method described in Section 3 and in Appendix A. As before, we distinguish between two phases of the fluid motion for a given particle.

During erosional phases, when $|u_L| > u_e$, the solutions have the form $c_L = \Theta_e(t, t_k) + c_k \Omega_e(t, t_k)$, where Θ_e and Ω_e are defined in terms of integrals of a_e and b_e as in Section 3 and Appendix A. (Ω_e may be expressed in terms of elementary functions, while Θ_e cannot but may readily be evaluated numerically.)

During purely depositional phases, when $|u| < u_e$, the solutions can be expressed as $c_L = c_d \Omega_d(t, t_d)$, where Ω_d is defined as in Appendix A and may be evaluated as an exponential of elementary functions.

As before, we construct the Lagrangian solution in each interval in turn, then identify the concentrations at the start and end of an oscillation to obtain a periodic solution, and finally substitute in for the labelling quantity $r_0(r, t)$ using Eq. (42) to obtain the Eulerian solution $c(r, t)$.

4.2. Typical solutions

As before, we concentrate attention on case (i) for the two values of the erosion exponent $n = 1$ and $n = 3$, and then comment on the effect of altering the sediment grain size \hat{D}_s .

4.2.1. Reference case (i)

Figs. 15 and 16 show the suspended sediment concentration for the reference cases, while Fig. 17 shows the corresponding patterns of net sediment transport.

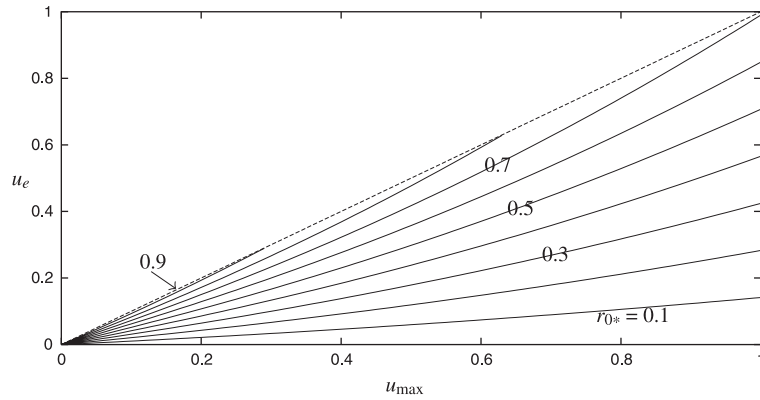


Fig. 13. Selected contours of $r_{0*}(u_{max}, u_e)$ (solid lines), together with the boundary $u_e = u_{max}$ of the regime in which sediment can be mobilised (dashed line). Lowest line represents $r_{0*} = 0.1$, uppermost represents $r_{0*} = 0.9$.

For both values of n , the principal features of the concentration field are a pronounced concentration maximum at or near the shoreline and a gradual decay of concentrations towards the inner limit of the active region $r = r_{0*}$, where velocities are no longer sufficient to mobilise sediment. As before, concentrations for $n = 3$ are considerably higher, which is essentially an artefact of the nondimensionalisation; a genuine difference between the cases is that, as before, concentrations associated with the concentration maximum are increased rather more than those in the body of the flow because increasing n increases the maximum value of the instantaneous equilibrium concentration c_{eq} more than the long-term mean concentration c_T . A

consequence of this is that the decay of c towards r_{0*} is rather stronger for higher n .

The principal feature of the radial sediment flux $Q(r)$ is a pronounced peak around the mean position of the shoreline: $Q(r)$ falls away steeply at either side of this and decays to zero as $r \rightarrow r_{0*}$. The decay is very much weaker inward of $r \approx 0.9$, which corresponds to the innermost position of the shoreline. Comparing Fig. 17a and b, the most obvious difference is that the higher value of n results in a noticeable region of inward net sediment transport around $r = 0.9$, whereas for $n = 1$, the region in which $Q < 0$ is much smaller and is located further inwards, around $r = 0.4$.

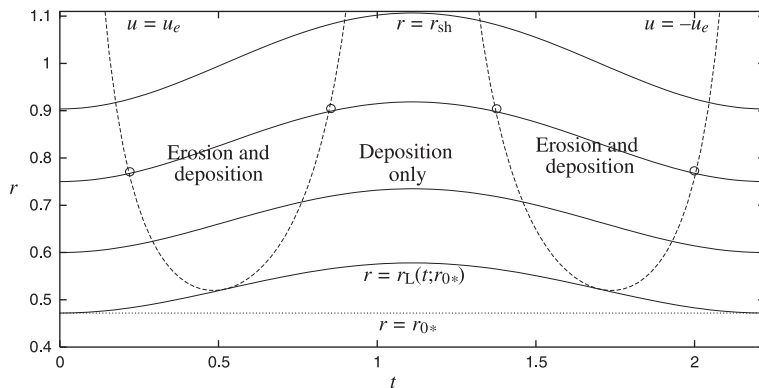


Fig. 14. Plot illustrating the Lagrangian form of Thacker's radial solution in a circular basin, for $\alpha = 0.2$. Solid lines represent particle trajectories $r_L(t)$, with the uppermost representing the shoreline $r_{sh}(t)$ and the lowermost representing $r_{in}(t)$. The dashed lines represent solutions of $u(r, t) = u_e = 0.15$. The small open circles \circ represent, respectively, t_{e1} , t_{e2} , t_{e3} , and t_{e4} for the particular fluid element with $r_0 = 0.75$. For further clarification, see text.

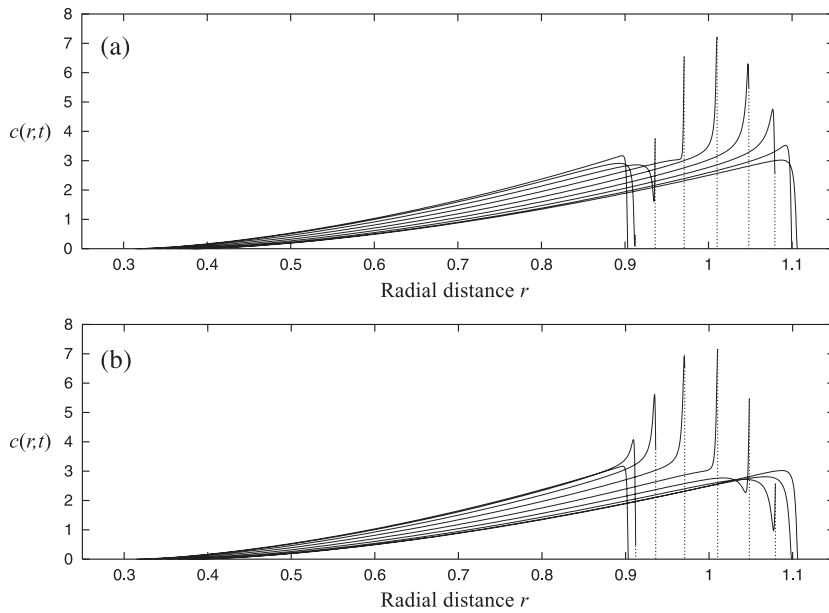


Fig. 15. Analytical solution for suspended sediment concentration under radial flow, for case (i) with $n=1$. (a) Outward flow; (b) inward flow.

This spatial pattern of net transport may be explained as follows. In the outermost inundated portion of the basin, there is a supply of sediment from the high concentrations at and behind the shore-

line, and suspension lag leads to a net outwards flux (as in Section 3), as material eroded on the outflow settles out at slack water, giving lower concentrations on the inflow. In the region inwards of $r=1$, the

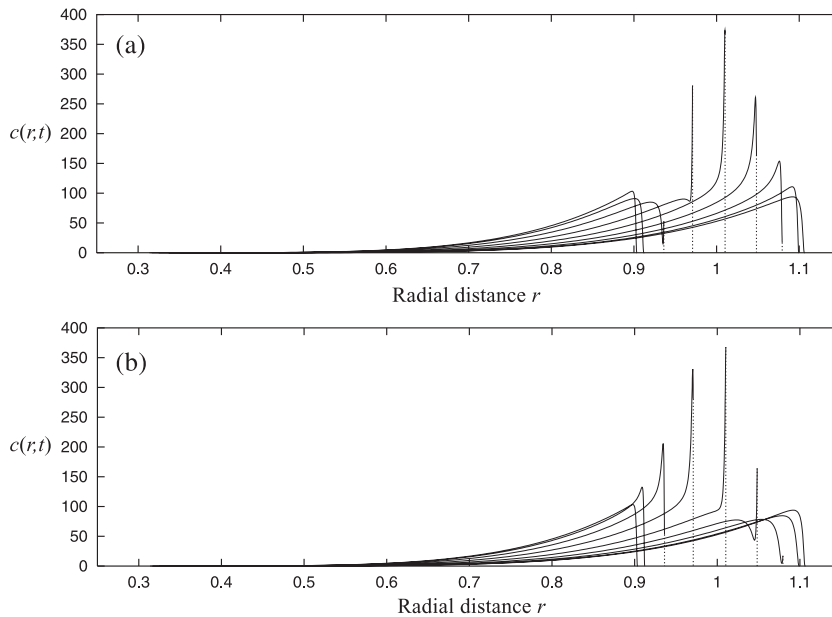


Fig. 16. Analytical solution for suspended sediment concentration under radial flow, for case (i) with $n=3$. (a) Outward flow; (b) inward flow.

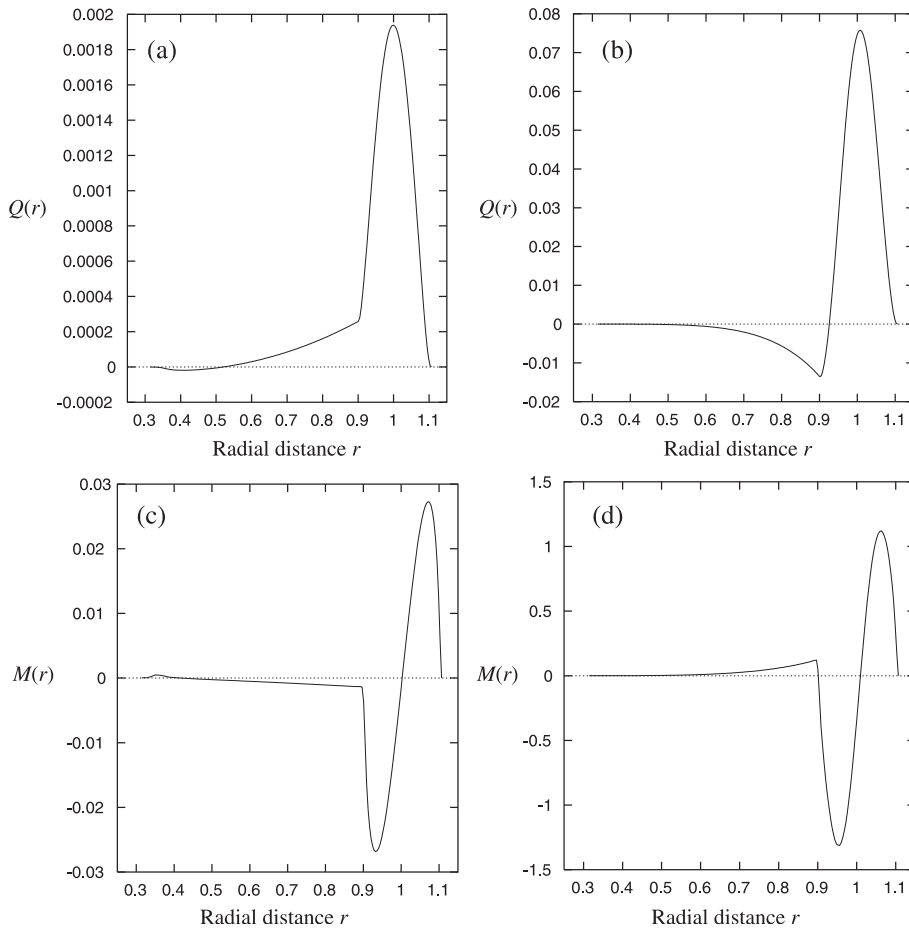


Fig. 17. Residual net sediment flux $Q(r)$ and net deposition $M(r)$ under radial seiching flow, for case (i) with $n=1$ (a, c) and for $n=3$ (b, d). The maximum bed level change for $n=1$ is $|\dot{Z}_c| \approx 8$ mm, and for $n=3$ is $|\dot{Z}_c| \approx 1.3$ cm, each over 1 hour.

growing concentration maximum on the inflow causes a peak inward flux which increases strongly with decreasing r ; however, the peak outward flux varies more weakly over this range because during the erosive phase, lower concentrations are being advected outwards from the region near r_{0^*} . The effect of this is that the inward fluxes eventually become large enough to overwhelm the outward fluxes and lead to a net inwards movement of sediment in this region. Both outward and inward fluxes gradually decrease with decreasing r as mean concentrations fall, and so the net flux decays towards zero at $r=r_{0^*}$.

Despite the differences in the patterns of net flux for the two values of n , the overall patterns of erosion and deposition (Fig. 17c and d) are rather similar, with

material being eroded from an annular region just outward of the position of maximum run-down and deposited principally higher up the sides of the basin. The major difference which the erosion formulation makes is to the amount of material which is deposited towards the centre of the basin: for $n=1$, this quantity is practically negligible and is deposited far inwards, while for $n=3$, a noticeable ‘lip’ of deposited material forms just inwards of the eroded annulus. If these transport patterns persist for long periods, we might expect the formation of a formation resembling a beach step around the mean position of the shoreline; however, it is likely that before such a feature forms, the hydrodynamics will be significantly affected by the more complex bathymetry.

4.2.2. Effect of varying the particle size

The general trends in the net sediment transport as the parameters α and u_c are varied are the same as under axial flow and may be explained in the same way: we therefore omit them here for brevity. However, it is again valuable to consider the variation of the transport patterns with \hat{D}_s : this is shown in Fig. 18.

The broad pattern of erosion and deposition is qualitatively the same for all sediment sizes, with significant deposition towards the outside of the basin, slight deposition nearer the centre, and an eroded annulus in-between. However, it varies significantly in both magnitude and position as \hat{D}_s is varied.

As \hat{D}_s is increased, the critical velocity for erosion u_c increases somewhat, and so the inner boundary of the active region $r=r_{0*}$ moves outwards. (This is particularly evident for the coarser grain sizes, cases (ii) and (iv) in Fig. 18.) At the same time, the bed exchange rate E increases strongly, so suspension lag

becomes more effective in deeper water. The net effect of these two processes is to compress the pattern of erosion and deposition into a narrower annulus; the reduced distance between the eroded region and the inner boundary also encourages deposition towards the centre of the basin at maximum run-down, so that for the coarsest sediment considered (case (ii) in Fig. 18), this deposit is comparable to that in the outer part of the basin.

It is interesting to note that despite the different hydrodynamics, the rates of erosion and deposition are comparable to those under axial flow (Section 3). The maximum rate of bed level change again occurs for $\hat{D}_s=0.2$ mm (case (iv) in Fig. 18) and is again approximately 5 cm over an hour of seiching. This supports the consistency of this approach as a way of estimating the morphodynamical importance of seiching motions, even when the precise details of the hydrodynamics are rather more complex than those considered here.

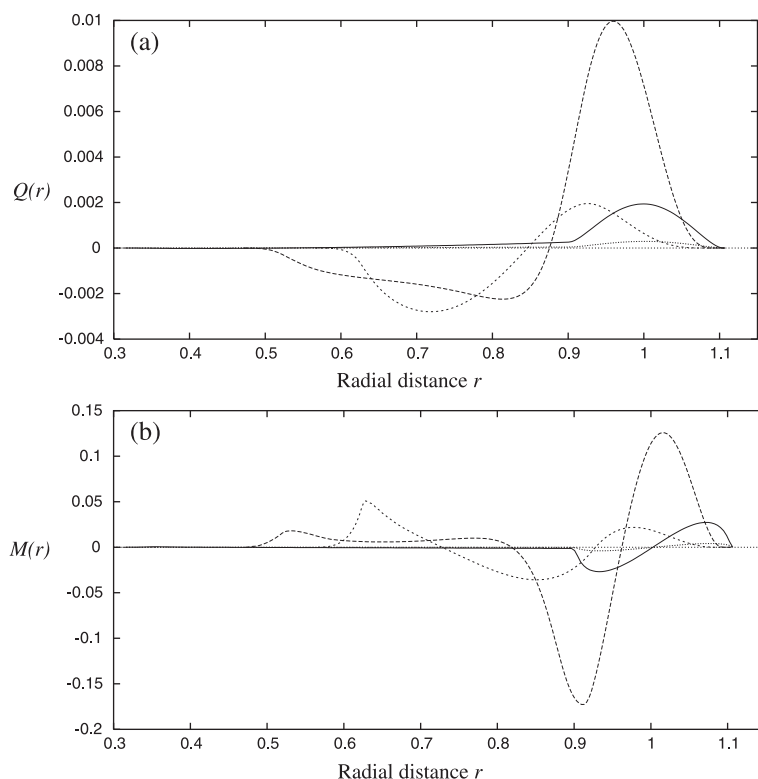


Fig. 18. (a) Residual net sediment flux $Q(r)$ and (b) net deposition $M(r)$ under radial seiching flow, for case (i) (solid line); case (ii) (light dashed line); case (iii) (dotted line); case (iv) (heavy dashed line). The exponent $n=1$ in each case.

5. Discussion and conclusions

The principal finding of this study is that a characteristic pattern of net sediment transport is associated with each of the modes of oscillation considered. When flow is parallel to one axis of the basin, material is transported exclusively from deeper to shallower parts of the basin, leading to erosion in the interior and deposition around the edges of the basin. In contrast, radial flow leads to slight deposition in the centre of the basin and substantial deposition around the edges, while material is eroded from the annular region in-between.

This general pattern of transport is highly robust to most of the physical parameter values as well as to the sediment entrainment relation employed, suggesting that it has genuine physical significance. Both the net rate and, to a lesser extent, the spatial pattern of erosion and deposition are influenced strongly by the sediment grain size \hat{D}_s , which controls the time taken for the suspended sediment concentration to respond to changes in the fluid velocity. This offers the possibility of seiching as a mechanism to explain the segregation of different types of sediment; we note that the behaviour of a multimodal sediment regime could be addressed directly using the method described here.

The patterns of sediment transport described here may be explained in terms of the mechanisms of suspension lag. When offshore concentrations are maintained, so there is a supply of sediment to the nearshore region, the settling of material from suspension at high water tends to move sediment from deeper to shallower regions, as occurs in a number of other coastal situations (Nichols and Biggs, 1985; Pritchard and Hogg, submitted for publication (a)). However, when offshore concentrations are low or vanished, for example, due to the presence of a local minimum in the velocity field, the lag effect tends to import sediment into the low-concentration region as well: a similar process was predicted under cross-shore standing waves by Pritchard and Hogg (submitted for publication (b)). Because deeper water in the offshore region leads to a slower sediment response at slack water, the offshore flux of sediment in this region is rarely as strong as the onshore flux in the nearshore.

The exact solutions presented here apply only to a highly idealised bathymetry. However, the mechanism

which they elucidate is clearly rather more general. We believe therefore that it offers insight into the role which seiching motions may play in the morphodynamics of enclosed bodies such as lagoons and harbours even when the bathymetry is more complex. In particular, it offers a route by which fine sediment may be transported up the bed slope of the basin, possibly returning back to the deeper regions in the form of bedload (or, for cohesive sediment, of downslope flows of fluid mud).

The solutions presented here have both quantitative and qualitative applications. They allow the morphodynamic importance of seiching motions to be estimated by providing quantitative estimates of the amount of transport which suspension lag can produce under these flows: we find that seiches may be an especially important mechanism for sediment in the size range of fine sand, for which bed level changes may be as much as several centimetres an hour. Additionally, these solutions offer a means by which observed erosion and deposition patterns may be linked to the principal modes of seiching. This supplies the engineer with a qualitative tool to supplement numerical simulations in determining the processes which lead to a given desirable or undesirable pattern of sedimentation.

From the perspective of numerical modelling, the solutions presented here appear highly suitable as test cases against which to validate numerical schemes. In particular, they complement Thacker's hydrodynamic solutions which, with their moving shoreline in two dimensions, already present a stern test of such schemes. The well-defined equilibrium concentration at the shoreline and the sharp concentration maximum provide a good test of the numerical representation of the concentration field in this region, and the ease with which net fluxes Q may be obtained offers a simple means of verifying the global predictions of a numerical model of sediment transport. They therefore represent a useful complement to the hindcasting studies which are generally used to validate sediment transport simulations. (We further note that the method described here for constructing exact solutions is not restricted to the description of sediment entrainment and deposition described here, but may be extended to a wide range of more complex models.)

Some interesting possibilities exist to extend the current study. Under certain restrictions (for example,

requiring a planar rather than a quadratic free surface), the governing equations from which Thacker's (1981) solutions arise become linear, and so two or more basic modes of oscillation may be combined to give a compound mode. For example, in an elliptical basin, solutions are available in which the fluid sloshes backward and forward in the x -direction with a dimensionless frequency $\omega_x = \sqrt{2}$ and in the y -direction with a dimensionless frequency $\omega_y = \sqrt{2}\hat{D}_y/\hat{D}_x$, while the free surface remains planar. In principle, exact solutions for sediment transport under these flows could be constructed and investigated in the same manner as the current paper. In practice, while it is easy to cast the hydrodynamics in Lagrangian form, the bookkeeping required to locate the appropriate erosional and depositional phases may become prohibitively complicated. (The reader is referred to the study by Shapiro (1996) for an illustration of the fluid trajectories which must be considered.) Results could, however, readily be obtained by numerical integration of the governing equations in Lagrangian form (as for Pritchard and Hogg, submitted for publication (b)), and this would make an interesting topic for further investigation.

Acknowledgements

AJH acknowledges the financial support of EPSRC; DP acknowledges the support of EPSRC and of the BP Institute. We would like to thank two anonymous referees for their constructive comments.

Appendix A. Constructing periodic solutions for suspended sediment concentration

We write the equation governing the concentration history of a fluid element labelled by \mathbf{x}_0 as

$$\frac{dc_L}{dt}(t; \mathbf{x}_0) = a(t; \mathbf{x}_0) - b(t)c_L(t; \mathbf{x}_0). \quad (50)$$

The only constraint this places on the bed exchange terms q_e and q_d is that q_d is proportional to c . In particular, it could readily be applied to models which include a time-varying vertical concentration profile

in each fluid element, so that \mathcal{C}_b is explicitly a function of t .

Eq. (50) is linear in c_L , and so the solution satisfying the initial condition $c_L(t_0) = c_0$ may be written as

$$c_L(t; t_0) = \Theta(t, t_0) + c_0\Omega(t, t_0), \quad (51)$$

where

$$\begin{aligned} \Theta(t, t_0) = & \exp\left(-\int_{t_0}^t b(t')dt'\right) \\ & \times \int_{t_0}^t \exp\left(\int_{t_0}^{\tau} b(t')dt'\right) a(\tau)d\tau \end{aligned} \quad (52)$$

and

$$\Omega(t, t_0) = \exp\left(-\int_{t_0}^t b(t')dt'\right). \quad (53)$$

We then construct a periodic solution by requiring $c(t) = c(t+T)$, where T is the period: rearranging for $c(t)$, we then obtain

$$c(t) = \frac{\Theta(t+T, t)}{1 - \Omega(t+T, t)}. \quad (54)$$

Depending on the exact forms of $a(t)$ and $b(t)$, it may not be possible to express the integrals $\Omega(t, t_0)$ and $\Theta(t, t_0)$ in terms of elementary functions. (When this is possible, as in Section 3, it is generally achieved by dividing the period into separate erosional and deposition intervals and obtaining Θ and Ω corresponding to the appropriate forms of a and b in each interval.) However, it is generally straightforward to evaluate it numerically. The solutions plotted in this paper were evaluated using standard integration routines (Press et al., 1992) implemented in FORTRAN 77 or in the computer algebra packages MAPLE 6 and 7.

Appendix B. Quantifying the effects of friction

Throughout this study, we have neglected the effect of friction on the hydrodynamics and its consequences for sediment transport. This neglect is based on the fact that the ratio of frictional terms to advective acceleration terms in the momentum equation is

generally small. Assuming a Chezy drag law, we can define this ratio as

$$\Delta(x, t) \equiv \frac{K |\mathbf{u}|^2 / h}{|\mathbf{D}\mathbf{u}/Dt|}, \quad \text{where } \frac{D\mathbf{u}}{Dt} = \frac{\partial}{\partial t} + (\mathbf{u} \cdot \nabla)\mathbf{u}. \quad (55)$$

The condition $\Delta(x, t) > \epsilon$, for some small constant ϵ , then defines the region of the fluid domain where the approximation of neglecting friction is formally inaccurate—usually, this region is a narrow strip near the shoreline.

Without explicitly calculating hydrodynamic solutions which incorporate friction, we cannot precisely quantify the effect which it may have on the sediment transport processes. However, we can obtain a first-order estimate $\Delta_0(x, t)$ by evaluating Δ using just the frictionless hydrodynamic solutions. Typically, this provides a considerable overestimate of the importance of friction around points of maximum velocity, when the frictionless advective acceleration term vanishes: in a solution for the frictional hydrodynamics, the friction would induce a nonzero acceleration which would partially balance it. However, by using this overestimate, we can obtain a rather unforgiving test of our predictions for sediment transport. The simplest method is simply to calculate the net flux Q disregarding all sediment transport which occurs in the region $\Delta_0 > \epsilon$ and compare it with the net flux which occurs when friction is neglected to determine how much of the net transport occurs in the region where friction is negligible. If the majority of sediment transport occurs in this region, and if the pattern of net transport is substantially unaltered by neglecting the more frictional region, then we may conclude that our frictionless solutions offer useful insight into the more complex dynamics which would result when friction was included.

B.1. Axial flow in an elliptical basin

Under the axial flow of Section 3, the quantity $\Delta_0(\mathbf{x}, t)$ is given by

$$\Delta_0(\mathbf{x}, t) = \frac{1}{h} \left| \frac{KA \sin^2 \omega t}{\cos \omega t} \right|, \quad (56)$$

and so the condition $\Delta_0 > \epsilon$ corresponds to the region

$$|x_{\text{sh}}(t) - x| \leq \sqrt{1 - Y^2} \times \left| 1 - \sqrt{1 - \frac{KA}{\epsilon(1 - Y^2)} \frac{\sin^2 \omega t}{\cos \omega t}} \right|. \quad (57)$$

Employing Eq. (57), we find that the sharp shoreline peak in c evident in Fig. 4 lies mostly in the region where $\Delta \geq 0.1$ during most of the oscillation, even for $Y=0$, and so we may expect the effect of friction to be noticeable in the concentration field and to significantly reduce the maximum concentrations in the nearshore region.

However, the effect on the net fluxes is less profound: because of the decreasing depth of the fluid towards the shoreline, the sediment load ch does not have a local maximum near the shoreline, and in fact tends to zero there, contributing only weakly to the net flux. Inspection of plots of $\mathbf{q}(x, Y, t)$ and of $Q(x, Y)$ reveals that the majority of net sediment transport takes place in regions where $\Delta_0 < 0.2$, and that the distribution of net sediment transport is qualitatively unaltered even if the region in which $\Delta_0 > 0.2$ is entirely omitted from the integration; the only exception to this is close to the edge of the basin $Y \approx 1$, where fluid remains shallow throughout the oscillation and we may expect the hydrodynamics to differ somewhat from the frictionless solutions of Thacker (1981).

Overall, despite our reservations about the validity of our solutions close to the shoreline, we can be reasonably confident that the introduction of friction to the model would involve only a small correction to the pattern of net sediment transport under this mode of flow.

B.2. Radial flow in a circular basin

Under the radial flow described in Section 4, we may evaluate the quantity $\Delta_0(r, t)$ as

$$\Delta_0(r, t) = \left| \left[\frac{2K\alpha^2 r^2 \sin^2 \sqrt{8}t}{\sqrt{1 - \alpha^2(1 - \alpha \cos \sqrt{8}t)} - (1 - \alpha^2)r^2} \right] \times \left[\frac{(1 - \alpha \cos \sqrt{8}t)^2}{r[2\alpha \sin^2 \sqrt{8}t - 4(\alpha - \cos \sqrt{8}t)]} \right] \right| \quad (58)$$

It is again straightforward, though algebraically cumbersome, to solve the equation $\Delta_0 = \epsilon$ for r and thus to identify the region in which frictional effects may be significant.

Referring to our reference case (Fig. 15), it is easy to determine that, as in Section 3, the sharply defined concentration maximum lies largely within the frictional region, and so we may expect this feature to be noticeably reduced by frictional effects. However, the total quantity of sediment which this represents is not substantial.

We may also, as before, consider the effect on the net fluxes of neglecting transport in regions where $\Delta_0 > \epsilon$. As before, we find that this may reduce the peak values of the integrated fluxes Q somewhat, but does not substantially affect the pattern of transport. The effect is strongest for low values of E , for which lag effects are associated most strongly with very shallow water; it is therefore smallest when the sediment fluxes involved are most morphodynamically important.

References

- Ali, K.H.M., Crapper, M., O'Connor, B.A., 1997. Fluid mud transport. Proceedings of the Institution of Civil Engineers. Water, Maritime and Energy 124, 64–78.
- Allen, J.R.L., 1985. Principles of Physical Sedimentology. Allen and Unwin, London.
- Bartholdy, J., 2000. Processes controlling import of fine-grained sediment to tidal areas: a simulation model. In: Pye, K., Allen, J. (Eds.), Coastal and Estuarine Environments: Sedimentology, Geomorphology and Geoarchaeology. Special Publications, vol. 175. Geological Society, London, pp. 13–29.
- Batchelor, G.K., 1967. An Introduction to Fluid Dynamics. Cambridge Univ. Press, Cambridge.
- Bloesch, J., 1995. Mechanisms, measurement and importance of sediment resuspension in lakes. Marine and Freshwater Research 46, 295–304.
- Brocchini, M., Bernetti, R., Mancinelli, A., Albertini, G., 2001. An efficient solver for nearshore flows based on the WAF method. Coastal Engineering 43 (2), 105–129.
- Carrier, G.F., Greenspan, H.P., 1958. Water waves of finite amplitude on a sloping beach. Journal of Fluid Mechanics 4, 97–109.
- Chapon, E., Beck, C., Pourchet, M., Deconinck, J.-F., 1999. 1822 earthquake-triggered homogenite in Lake Le Bourget (NW Alps). Terra Nova 11, 86–92.
- Christie, M.C., Dyer, K.R., 1998. Measurements of the turbid tidal edge over the Skeffling mudflats. In: Black, K.S., Paterson, D.M., Cramp, A. (Eds.), Sedimentary Processes in the Intertidal Zone. Special Publications Geological Society, London, pp. 45–55.
- Dyer, K.R., 1986. Coastal and Estuarine Sediment Dynamics. Wiley, Chichester.
- Dyer, K.R., Soulsby, R.L., 1988. Sand transport on the continental shelf. Annual Review of Fluid Mechanics 20, 295–324.
- Einstein, H.A., Krone, R.B., 1962. Experiments to determine modes of cohesive sediment transport in salt water. Journal of Geophysical Research 67, 1451–1461.
- Garcia, M., Parker, G., 1991. Entrainment of bed sediment into suspension. ASCE Journal of Hydraulic Engineering 117 (4), 414–435.
- Le Hir, P., et al., 2000. Characterization of intertidal flat hydrodynamics. Continental Shelf Research 20, 1433–1459.
- Nichols, M.M., Biggs, R.B., 1985. Estuaries. In: Davis, R. (Ed.), Coastal Sedimentary Environments, 2nd ed. Springer-Verlag, New York. Chapter 2.
- Peregrine, D.H., 1972. Equations for water waves and the approximations behind them. In: Meyer, R. (Ed.), Waves on Beaches and Resulting Sediment Transport. Academic Press, New York, pp. 95–121. Chapter 3.
- Peregrine, D.H., Williams, S.M., 2001. Swash overtopping a truncated plane beach. Journal of Fluid Mechanics 440, 391–399.
- Press, W.H., Teukolsky, S.A., Vetterling, W.T., Flannery, B.P., 1992. Numerical Recipes in Fortran 77, 2nd ed. Cambridge Univ. Press, Cambridge.
- Pritchard, D., Hogg, A.J., 2003a. Cross-shore sediment transport and the equilibrium morphology of mudflats under tidal currents. Journal of Geophysical Research (in press).
- Pritchard, D., Hogg, A.J., 2003b. On fine sediment transport by long waves in the swash zone of a plane beach. Journal of Fluid Mechanics (in press).
- Pritchard, D., Hogg, A.J., Roberts, W., 2002. Morphological modelling of intertidal mudflats: the role of cross-shore tidal currents. Continental Shelf Research 22 (11–13), 1887–1895.
- Roberts, W., 1993. Development of a mathematical model of fluid mud in the coastal zone. Proceedings of the Institution of Civil Engineers. Water, Maritime and Energy 101, 173–181.
- Roberts, W.R., Le Hir, P., Whitehouse, R.J.S., 2000. Investigation using simple mathematical models of the effect of tidal currents and waves on the profile shape of intertidal mudflats. Continental Shelf Research 20, 1079–1097.
- Sanford, L.P., Maa, J.P.-Y., 2001. A unified erosion formulation for fine sediments. Marine Geology 179, 9–23.
- Schuttelaars, H.M., 1998. Nonlinear, long term equilibrium profiles in a short tidal embayment. In: Dronkers, J., Scheffers, M. (Eds.), Physics of Estuaries and Coastal Seas. Balkema, Rotterdam, pp. 337–343.
- Schuttelaars, H.M., de Swart, H.E., 1996. An idealised long-term morphodynamic model of a tidal embayment. European Journal of Mechanics. B, Fluids 15 (1), 55–80.
- Schuttelaars, H.M., de Swart, H.E., 1999. Initial formation of channels and shoals in a short tidal embayment. Journal of Fluid Mechanics 386, 15–42.
- Seminara, G., 2001. Invitation to sediment transport. In: Balmforth, N., Provenzale, A. (Eds.), Geomorphological Fluid Mechanics. Lecture Notes in Physics, Chapter 16. Springer, Berlin, pp. 394–402.
- Shapiro, A., 1996. Nonlinear shallow-water oscillations in a para-

- bolic channel: exact solutions and trajectory analyses. *Journal of Fluid Mechanics* 318, 49–76.
- Shteinman, B., Eckert, W., Kaganowsky, S., Zohary, T., 1997. Seiche-induced resuspension in Lake Kinneret: a fluorescent tracer experiment. *Water, Air and Soil Pollution* 99, 123–131.
- Soulsby, R.L., 1997. *Dynamics of Marine Sands: A Manual for Practical Applications*. Thomas Telford, London.
- Thacker, W.C., 1981. Some exact solutions to the nonlinear shallow-water wave equations. *Journal of Fluid Mechanics* 107, 499–508.